BRNO UNIVERSITY OF TECHNOLOGY

VYSOKÉ UČENÍ TECHNICKÉ V BRNĚ

FACULTY OF MECHANICAL ENGINEERING

FAKULTA STROJNÍHO INŽENÝRSTVÍ

INSTITUTE OF PHYSICAL ENGINEERING

ÚSTAV FYZIKÁLNÍHO INŽENÝRSTVÍ

POSSIBILITIES OF PREPARING NANOELECTRONIC DEVICES ON GRAPHENE USING AFM

MOŽNOSTI PŘÍPRAVY NANOELEKTRONICKÝCH ZAŘÍZENÍ NA GRAFENU POMOCÍ AFM

MASTER'S THESIS

DIPLOMOVÁ PRÁCE

AUTHOR — Bc. Daniel Lipták

AUTOR PRÁCE

SUPERVISOR — doc. Ing. Miroslav Bartošík, Ph.D.

VEDOUCÍ PRÁCE

BRNO 2023

BRNO UNIVERSITY OF TECHNOLOGY FACULTY OF MECHANICAL ENGINEERING

Assignment Master's Thesis

Institut:	Institute of Physical Engineering
Student:	**Bc. Daniel Lipták**
Degree programm:	Physical Engineering and Nanotechnology
Branch:	no specialisation
Supervisor:	**doc. Ing. Miroslav Bartošík, Ph.D.**
Academic year:	2022/23

As provided for by the Act No. 111/98 Coll. on higher education institutions and the BUT Study and Examination Regulations, the director of the Institute hereby assigns the following topic of Master's Thesis:

Possibilities of preparing nanoelectronic devices on graphene using AFM

Brief Description:

Due to its unique electronic properties: high mobility of charge carriers, the ability to influence the type of charge carriers by an external electric field, long spin decoherence times and low electronic noise, graphene is predestined for applications in the field of classical electronics such as high–frequency transistors, photodetectors, sensors and biosensors, but also with potential in the field of quantum computers. In order to use graphene in these devices, it needs to be laterally shaped using a suitable lithographic technique. In this context, a classic optical lithography no longer achieves sufficient resolutions, and electron lithography in turn undesirably affects the underlying graphene insulating substrates (e.g. SiO2 or hBN) by electrons. For these reasons, the possibility of lateral shaping of graphene using the local anodic oxidation (LAO) technique by atomic force microscope (AFM) will be tested in this thesis. This technique should achieve nanometer resolutions and minimal influence on the substrate. However, the question is, whether the insulating ability of oxide barriers will be sufficient for utilization in nanoelectronic devices. The answer to this question is to be sought in this diploma thesis.

Master's Thesis goals:

1. Do research on the mentioned issue.
2. Prepare suitable micrometer–sized Hall bars in a bottom solid–state gate FET arrangement.
3. Perform the fabrication of the following lithographic structures using LAO

a. Line interruption
b. Multiple interruptions
c. Area interruption
d. Constriction (in a shape of a quantum point contact).

4. Test the insulating effectiveness of barriers and charge propagation in fabricated structures using simultaneous transport measurements and KPFM.

Recommended bibliography:

GEIM, A. a K. NOVOSELOV. The rise of graphene. Nature Materials. 2007, 6(3), 183–191. ISSN 1476-1122. Dostupné z: https://doi.org/10.1038/nmat1849

OVERWEG, Hiske, et al. Electrostatically induced quantum point contact in bilayer graphene. ArXiv.org. 2018, 18(1), 553–559. ISSN 15306984. Dostupné z: https://doi.org/10.1021/acs.nanolett.7b04666

KONEČNÝ, Martin, et al. Kelvin Probe Force Microscopy and Calculation of Charge Transport in a Graphene/Silicon Dioxide System at Different Relative Humidity. ACS applied materials & interfaces. 2018, 10(14), 11987-11994. ISSN 19448244. Dostupné z: https://doi.org/10.1021/acsami.7b18041

Deadline for submission Master's Thesis is given by the Schedule of the Academic year 2022/23

In Brno,

L. S.

prof. RNDr. Tomáš Šikola, CSc. Director of the Institute	doc. Ing. Jiří Hlinka, Ph.D. FME dean

ABSTRACT

In this master's thesis, we focused on the study and preparation of nano-structures on graphene by local anodic oxidation. Our attention was put on the isolating capabilities of oxidized graphene, which was studied by surface electric potential mapping, using Kelvin probe force microscopy, with simultaneous transport measurement. The obtained results indicate the doubling of resistance by line interruption oxidation. Finally, nanoconstriction of micrometer dimensions was fabricated and studied under different relative humidities, in the range of 3% to 60%.

ABSTRAKT

V tejto diplomovej práci sme sa zamerali na štúdiu a prípravu nano-štruktúr na graféne pomocou lokálnej anodickej oxidácie. Naša pozornosť bola venovaná izolačným schopnostiam oxidovaného grafénu, ktorý bol študovaný pomocou mapovania povrchového napätia, využívaním sondovej mikroskopie Kelvinovej sily, a súčasným meraním toku nosičov nábojov. Získané výsledky poukazujú na zdvojnásobnenie odporu pri čiarovom oxidovom prerušení. Ku koncu, nano-zúženie s mikrometrovými rozmermi bolo vyrobené a študované pod rôznymi vlhkosťami, v rozmedzí 3% až 60%.

KEYWORDS

AFM, graphene, local anodic oxidation, KPFM

KĽÚČOVÉ SLOVÁ

AFM, grafén, lokálna anodická oxidácia, KPFM

LIPTÁK, D. *Possibilities of preparing nanoelectronic devices on graphene using AFM* Brno: Vysoké učení technické v Brně, Fakulta strojního inženýrství, 2023. 57 s. Vedoucí práce: doc. Ing. Miroslav Bartošík, Ph.D.

Author's Declaration

Author:	Daniel Lipták
Author's ID:	211549
Paper type:	Master's Thesis
Academic year:	2022/2023
Topic:	Possibilities of preparing nanoelectronic devices on graphene using AFM

I declare that I have written this paper independently, under the guidance of the advisor and using exclusively the technical references and other sources of information cited in the paper and listed in the comprehensive bibliography at the end of the paper.

As the author, I furthermore declare that, with respect to the creation of this paper, I have not infringed any copyright or violated anyone's personal and/or ownership rights. In this context, I am fully aware of the consequences of breaking Regulation § 11 of the Copyright Act No. 121/2000 Coll. of the Czech Republic, as amended, and of any breach of rights related to intellectual property or introduced within amendments to relevant Acts such as the Intellectual Property Act or the Criminal Code, Act No. 40/2009 Coll. of the Czech Republic, Section 2, Head VI, Part 4.

Brno ....

author's signature*

*The author signs only in the printed version.

ACKNOWLEDGEMENT

I would like to express my gratitude towards the supervisor of my thesis, doc. Ing. Miroslav Bartošík, Ph.D., who provided valuable insights into the theoretical background of the thesis topic. Profound respect and gratitude goes towards Bc. Linda Supalová, who provided us with the necessary samples for the experiments and the precise description of their preparation process. I would like to personally thank Ing. Martin Konečný, Ph.D. and Ing. Vojtěch Švarc, who provided valuable advice during both the theoretical and experimental parts of the thesis. Special thanks go to Bea, Pavel and Míša for sharing an office with me and helping during the writing process. Finally, I would like to thank my family and friends for supporting me, without whom this work would not have been possible.

Contents

Introduction **3**

1 Theory **5**
1.1 Graphene 5
1.1.1 Fundamentals of graphene 5
1.1.2 Geometric structure of graphene 6
1.1.3 Electronic description of graphene 7
1.1.4 Preparation of graphene by chemical vapor deposition 8
1.2 Lithography by atomic force microscopy 10
1.3 Kelvin probe force microscopy 12

2 Research **15**
2.1 Graphene mobility 15
2.2 Lithography on graphene 16
2.2.1 Lithography by AFM 16
2.2.2 Other lithography techniques 22
2.2.3 Graphene based sensors 24

3 Thesis results and experimental setup **27**
3.1 Sample fabrication and preparation 27
3.2 Experimental setup 31
3.3 Results 34
3.3.1 Hall probe main channel interruption 34
3.3.2 Constriction 39
3.3.3 Challenges 44

Conclusion **47**

Bibliography **49**

Abbreviations **55**

A Used AFM probes **57**

Introduction

Nanotechnology is becoming more and more a part of our day-to-day life. Such a field in technology deals with the fabrication and study of objects that have at least one of their dimensions in the nanometer range. The motivation behind this branch of science is the fact that the properties of materials in such arrangements can influence their properties on a larger scale, which may be exploited for advancements in technology. In order to characterize such materials, specialized techniques have been developed to gather information about their behaviour under controlled conditions or simply just to map their surface topography.

One of the most wide-spread methods of surface topography is scanning probe microscopy (SPM), which uses a probe with a sharp tip to scan the surface of a sample material. There are two main types of SPM techniques: scanning tunnelling microscopy (STM) and atomic force microscopy (AFM). In this master's thesis, we will be working with the latter, which uses inter-atomic forces between the tip and the sample, such as the van der Waals forces, to measure the topography. AFM is also capable of operating under atmospheric pressures and standard laboratory conditions.

In our case, the material of interest will be graphene, which is a 2D nanomaterial made of carbon, arranged in a hexagonal lattice. This allotrope of carbon has a number of interesting properties, which can be utilized to fabricate high precision sensors of humidity, biochemical sensors and to research fundamental phenomena, such as the Hall effect. The elementary research being particularly of interest for the building of alternative designs of quantum super computers.

To make such devices, one must first laterally shape the graphene into the desired designs. This necessary lithography can be done in a multitude of ways, including methods that use an AFM as a platform. Local anodic oxidation (LAO) is one such method, which allows us to locally oxidize selected areas of graphene. Since graphene is an electric conductor and graphene oxide is an insulator, electric nanodevices could be prepared by LAO. However, the isolating capabilities of graphene oxide have been largely unexplored.

This problem is addressed in this project. This work aims to perform LAO on graphene and characterize its isolation capability by mapping the surface electric potential of the affected and surrounding areas by Kelvin probe force microscopy. Simultaneously, transport measurements will be conducted on the samples to observe the changes in the resistance of graphene in real time.

This master's thesis is divided into three main chapters. In chapter 1, the theoretical background of graphene as a nanomaterial is explained, continued by the principle and inner workings of LAO. The chapter is concluded by the explanation

of Kelvin probe force microscopy (KPFM), which is an advanced technique using an AFM for the measurement of surface electric potential. In chapter 2, we provide research on the most relevant literature at hand, including graphene's properties, LAO and other lithography methods. Following the theoretical chapters, chapter 3 contains the preparation process of samples that were used during the project, the setup of the experimental measurements and the final results acquired throughout the thesis with a brief mention of the challenges we faced. Finally, the conclusion provides a summary of the master's thesis as a whole with our final thoughts.

1 Theory

In this chapter of the thesis, the theoretical background of the used materials and techniques will be introduced. The main material in question will be graphene and the two main techniques will be local anodic oxidation and Kelvin probe force microscopy. With this basic theoretical understanding, the following chapter, literature research, will be much better understood and given context.

1.1 Graphene

To understand graphene as a material, firstly, we will be describing its basic structure and what it is made out of. Secondly, the electronic properties will be stated, together with context as to why this material is being used in today's industry. Finally, the manufacturing process will be briefly described.

1.1.1 Fundamentals of graphene

Carbon is considered to be one of the most versatile elements in nature due to its extraordinary ability to form long chains of compounds. Such chains are possible, because carbon creates bonds with not only other elements, but also with itself [1]. There are several ways carbon can bond to other carbon atoms, forming materials (so called allotropes of carbon) with vastly different mechanical and electronic properties. Such allotropes are: diamond, graphite (3D bulk carbon) [2], graphene (2D carbon sheet), carbon nanotube (1D tube of twisted graphene) and fullerene (0D) [3].

The high bonding capability is present thanks to a phenomenon called hybridization. In its basic state, carbon contains two valence electrons in the $2p$ orbital. However, when the energy of the system is increased through external influences, an electron from the $2s$ orbital occupies a vacancy in the $2p$ orbital. This phenomenon increases the amount of possible bonds of carbon from two to four [4].

By being able to form up to four bonds with other atoms, carbon is the backbone of organic chemistry, where one of the basic building blocks is the benzene ring. This compound is a hexagonal ring made of carbon, where three electrons are used for the bonds between the carbon atoms and the remaining dangling bond is used to bind to hydrogen. Although the structure of graphene is similar in shape to the benzene ring in form, in graphene the double bond between carbon atoms is instead used to bind to other rings of carbon. The other difference between graphene and benzene rings is that the hydrogen atoms in graphene are not present and instead the free electron forms a two-dimensional electron gas on the surface of the material.

1.1.2 Geometric structure of graphene

Graphene as a material is a two-dimensional crystal of carbon atoms, which are periodically arranged in a hexagonal lattice. The sp^2 hybridization forms the σ covalent bond laying in plane with the material, which is responsible for the high mechanical strength. The $2p$ bond perpendicular to the plane of graphene leads to the formation of two π bands. These π bands determine the low-energy excitation of electrons of the material. The bonding and anti-bonding orbitals then form the valence and conduction bands of graphene. Another way of describing the structure of graphene is to think of it as a triangular lattice with a basis formed by two carbon atoms A and B [5]. Such atoms would then be given the lattice translation vectors $\vec{a}_1$ and $\vec{a}_2$ respectively:

$$\vec{a}_1 = \frac{a}{2}\left(3, \sqrt{3}\right), \qquad \vec{a}_2 = \frac{a}{2}\left(3, -\sqrt{3}\right), \tag{1.1}$$

where the distance a is the distance between two neighboring carbon atoms, which is roughly equal to 1.42 Å. The above mentioned vectors are ideal for describing the geometric structure of graphene in real space. However, for the description of the electronic properties materials, the reciprocal space is used. As such, the lattice vectors $\vec{b}_1$ and $\vec{b}_2$ are used with respect to the previous ones, where:

$$\vec{b}_1 = \frac{2\pi}{3a}\left(1, \sqrt{3}\right), \qquad \vec{b}_2 = \frac{2\pi}{3a}\left(1, -\sqrt{3}\right). \tag{1.2}$$

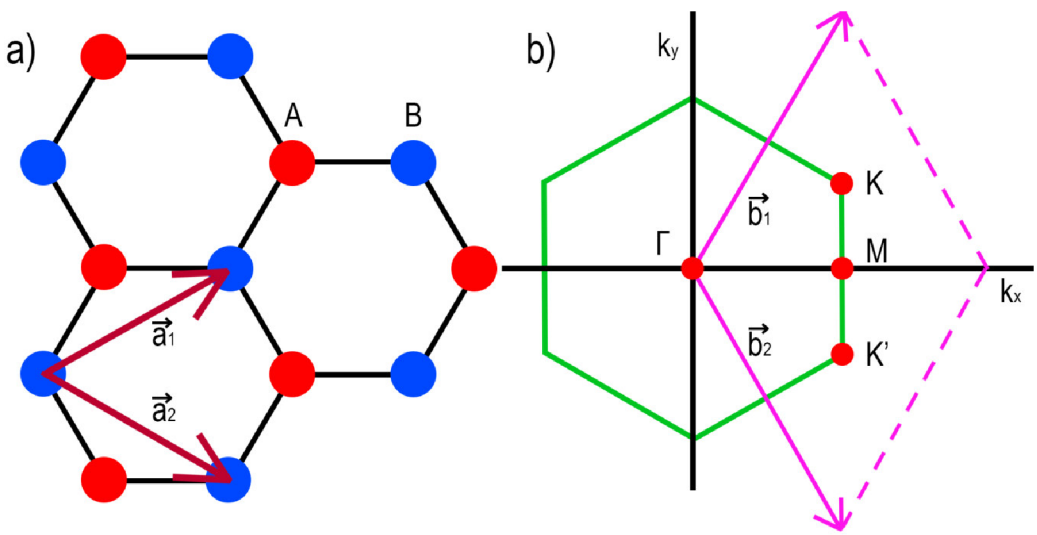

Fig. 1.1: Honeycomb lattice in real space (a) and its corresponding Brillouin zone (b) in reciprocal space.

For a better understanding of the position of the above mentioned vectors, an illustration is provided above (fig. 1.1). In fig. 1.1 (a), we can see the lattice vectors' positions ($\vec{a}_1$ and $\vec{a}_2$) in real space and in part (b) we can spot the reciprocal lattice vectors ($\vec{b}_1$ and $\vec{b}_2$). The points marked as K and K' are the so called Dirac points, which lie at the edges of the first Brillouin zone [7]. These points take significance when talking about the electronic properties of graphene. The position of points K and K' can be written in the reciprocal space as:

$$\mathrm{K} = \left(\frac{2\pi}{3a}, \frac{2\pi}{3\sqrt{3}a}\right), \qquad \mathrm{K'} = \left(\frac{2\pi}{3a}, -\frac{2\pi}{3\sqrt{3}a}\right). \tag{1.3}$$

1.1.3 Electronic description of graphene

In order to describe the behaviour of charge carriers around the Dirac point, certain approximations are used to ease the complexity of calculations. The tight-binding approximation would be the most prevalent, which ensure that only the nearest and second-nearest atoms would be considered in terms of interactions.

One of the ways to describe a material's electronic properties is to visualize its energy bands of the valence and conductive states. When it comes to graphene, the number of possible states around the Dirac point is strongly reduced. Therefore, graphene is a semimetal or semiconductor with zero band gap. In reciprocal space, the shape of the energy dispersion around the Dirac point is reminiscent of two cones touching at their vertices.

The tight-binding Hamiltonian for electrons in graphene leads to the polynomial dispersion relation:

$$E_{\pm}(k) = \pm t\sqrt{3 + f(k)} - t' f(k), \tag{1.4}$$

where t and t' are the nearest-neighbor hopping energy (hopping between different sublattices) and the next nearest-neighbor hopping energy (hopping within the same sublattice), respectively. The function $f(k)$ takes the following form:

$$f(k) = 2\cos\left(\sqrt{3}k_y a\right) + 4\cos\left(\frac{\sqrt{3}}{2}k_y a\right)\cos\left(\frac{3}{2}k_x a\right). \tag{1.5}$$

From equations 1.4 and 1.5, it is apparent that the energy spectrum is symmetrical around zero. However, this symmetry is only possible if t' equals to zero. For non-zero values, the electron-hole pair symmetry is broken and the valence and conductive bands become asymmetric. The near-linear profile of the dispersion around the Dirac point can be observed in Fig. (1.2):

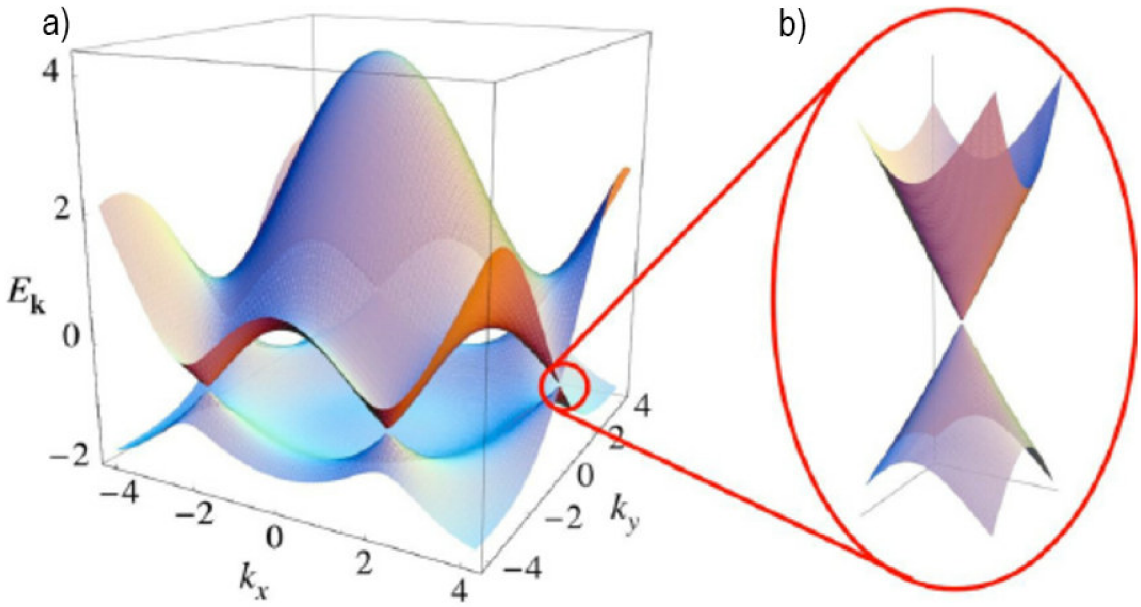

Fig. 1.2: Energy dispersion in the graphene honeycomb lattice. Left: energy spectrum in units of t, where t and t' are $t = 2.70\,\mathrm{eV}$ and $t' = 0.54\,\mathrm{eV}$. Right: detail the Dirac cone. Adapted from [3].

1.1.4 Preparation of graphene by chemical vapor deposition

The unique and highly valued properties of graphene have incentivized many studies, aiming to achieve new technological heights. However,in order to study the material and its applicability in modern times, one must obtain the material in the first place.

So far, the highest quality of graphene is achieved by mechanical cleavage of highly oriented pyrolytic graphite (HOPG). This method can be conducted even as simply as using scotch tape on the HOPG and tearing it off with a layer of graphite stuck on the tape. Another piece of tape would then be applied to the graphite contaminated side of the first tape. The process would iteratively arrive at single-layer graphite (graphene) which could be used for experimental purposes. However, the resulting graphene flakes are, for a large number of potential experiments, much too small in area and the time-consuming nature of the process makes the other methods seen as favorable by comparison.

One such method would be chemical vapor deposition (CVD) onto transitional metal substrates, such as Ni, Pd, Ru, Ir and Cu [8]. After heating up the substrate in high vacuum conditions a carbon source in the form of carbon vapor or hydrocarbons is introduced into the environment. Depending on the substrate material, one of two main phenomena can occur for the formation of a graphene monolayer [6].

The first one involves the carbon atoms combining with the substrate material,

forming a solution. The carbon atoms occupy vacancies in the crystalline structure of the material by diffusion. As the substrate is cooled down, the carbon atoms segregate onto the surface from the bulk material, forming graphene.

The second phenomenon is not reliant on diffusion. As the carbon source is introduced to the environment, a number of initial carbon atoms stick to the substrate. These atoms would then be the nuclei of graphene (this process is referred to as nucleation), as the following carbon atoms binding to the graphene nuclei would need less energy to stick to the substrate surface.

CVD is capable of producing high quality graphene, with charge carrier mobilities even up to $7350\,\mathrm{cm^2V^{-1}s^{-1}}$ (in comparison, the mobility of electrons in exfoliated graphene reaches up to $200000\,\mathrm{cm^2V^{-1}s^{-1}}$) [9], with graphene growth areas only limited by the substrate size. These qualities of CVD make the method preferred over the aforementioned exfoliation [10].

The two processes can be observed in Figure 1.3 below.

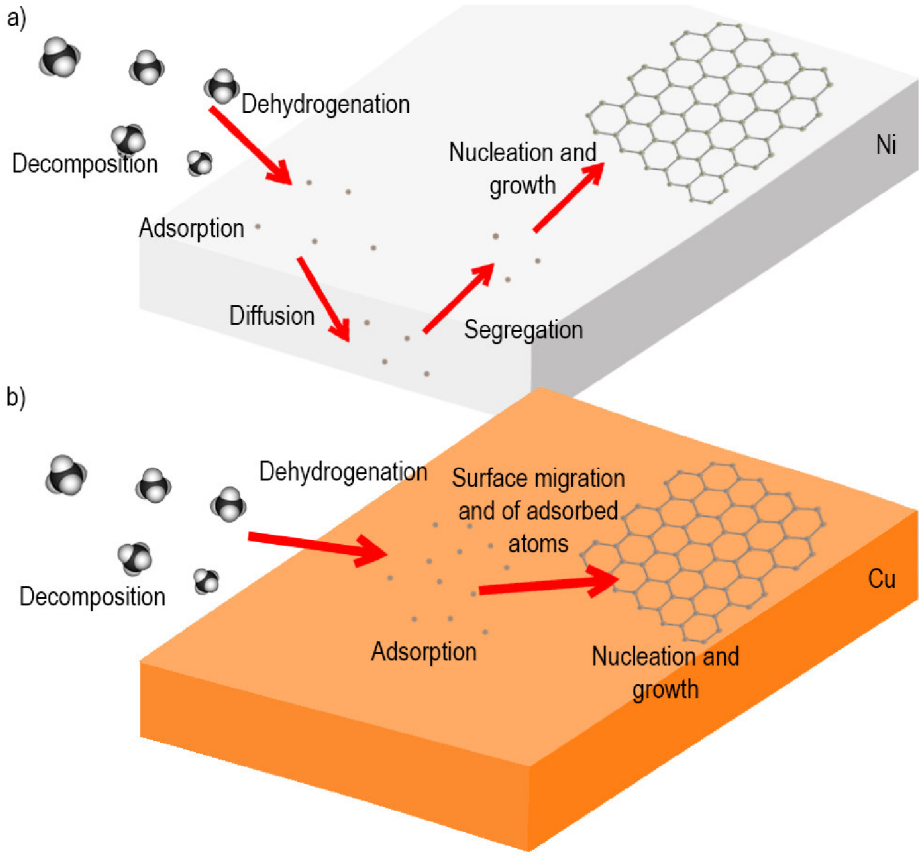

Fig. 1.3: Chemical vapor deposition of graphene on metal substrates: a) diffusion and segregation can be seen in the Ni substrate. b) adsorption and atomic migration can be seen on the Cu substrate.

1.2 Lithography by atomic force microscopy

The drive to create new technologies has led to the development of a diverse range of lithography techniques for their formation. As such, each lithography method has their own benefits and drawbacks. For example, photolithography involves the usage of resist covers, which are modified by a laser beam, after which the undesired parts of the substrate material are removed. The usage of such resists may cause fragmentation during the development in an unpredictable manner. Similar problems arise during electron-beam lithography. As a result, alternative methods of lithography have been devised, which avoid the usage of resists. One such method is local anodic oxidation, using an atomic force microscope.

Atomic force microscopy (AFM) is a type of scanning probe microscopy used for measuring the topography of a sample. The resulting images may achieve up to atomic resolutions, however, it is typically achieved under ultra-high vacuum (UHV) at low temperatures with an atomically sharp tip [11]. In ambient conditions, the resolution is lower depending on the tip apex, tip-sample water bridge (determined by relative humidity (RH)). Although the intended usage of AFM is to characterize the sample surface, other uses have been devised for the technique, such as lithography.

One of the simplest ways one can alter the topography of a sample is by mechanical lithography. This method involves using the cantilever tip of the probe to cleave through the sample target area by dragging the tip at a high contact force in contact mode [12]. The method itself, although simple, has a number of disadvantages, such as: possibly damaging more layers than originally intended, wearing out non-specialized probes and retaining fragments of the scratched material on the sample (see Fig.1.4) [13].

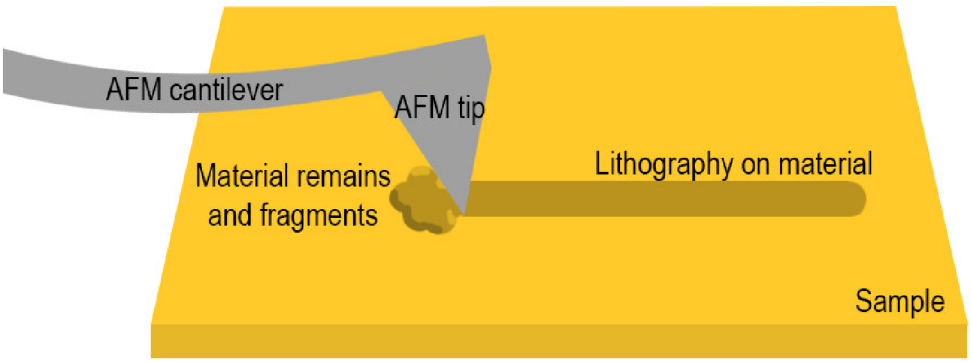

Fig. 1.4: Mechanical lithography done by AFM.

The other possible method of lithography by AFM is local anodic oxidation (LAO) [15]. This technique essentially changes the chemical composition of the sample on its surface by oxidation. The method requires the presence of water vapor in the form of high RH (approximately 30% - 60%), in order to form a water bridge between the AFM tip and the close-by sample area. By absorbing water molecules, the water bridge between the sample surface and the AFM tip forms in the shape of a meniscus [16]. When the sample is electrically grounded and a sufficient (threshold) voltage is applied to the AFM probe, the strong electric field in the water meniscus forms. When the negative voltage (oxidation voltage) is applied, oxyanions (OH^-, O^-) are driven towards the sample surface, which bind to the metallic material and form the oxide [17]. The following chemical reactions take place on a metallic substrate (M) [18]:

$$\mathrm{M} + n\mathrm{H_2O} \rightarrow \mathrm{MO}_n + 2n\mathrm{H}^+ + 2n\mathrm{e}^-$$
$$\mathrm{M}^n + 2n\mathrm{H_2O} + 2n\mathrm{e}^- \rightarrow n\mathrm{H_2} + 2n\mathrm{OH}^- + \mathrm{M},$$

while the remaining hydrogen atoms recombine into hydrogen gas as:

$$2\mathrm{H}^+ + 2\mathrm{e}^- \rightarrow \mathrm{H_2}.$$

The water meniscus shape and the scheme of the method can be observed in Fig. 1.5, where the bias voltage is the oxidation voltage and the sample is a metal, which can be oxidized.

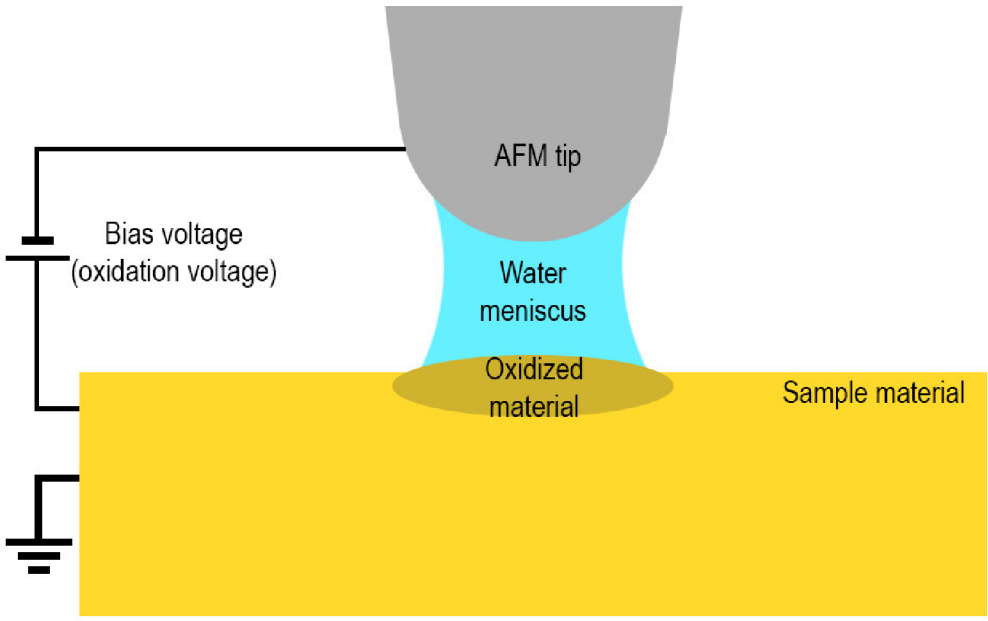

Fig. 1.5: Schematic representation of local anodic oxidation on a grounded metallic sample.

1.3 Kelvin probe force microscopy

AFM and other microscopy methods, such as scanning electron microscopy, have shown great capability in measuring the surface topography of samples made of a wide range of materials [19]. However, some samples may be heterostructural with no major differences in topography. In such cases, Raman spectroscopy would be a preferable alternative for determining the present materials. On the other hand, the structures may be simply too small in area for the method to be both reliable and precise. In such cases, measuring the surface electric potential of the given samples could be the most efficient method of characterization in the nanoscale [20].

One of the most popular techniques of determining the surface potential of a sample is Kelvin probe force microscopy (KPFM) [21]. The method itself measures a contact potential difference (CPD) [22] between the sample and the probe tip of an AFM with a conductive material. The CPD between the sample and the tip can be defined as:

$$V_{CPD} = \frac{\Phi_{tip} - \Phi_{sample}}{-e}, \tag{1.6}$$

where Φ_{tip} and Φ_{sample} are the work functions of the tip and the sample, respectively and e is the electronic charge. An electrical force is generated when the AFM tip is brought close to the sample surface, due to the differences in their Fermi energy levels. Fig. 1.6 depicts a series of energy level diagrams when the tip and sample work functions (Φ_{tip} and Φ_{sample}) are different.

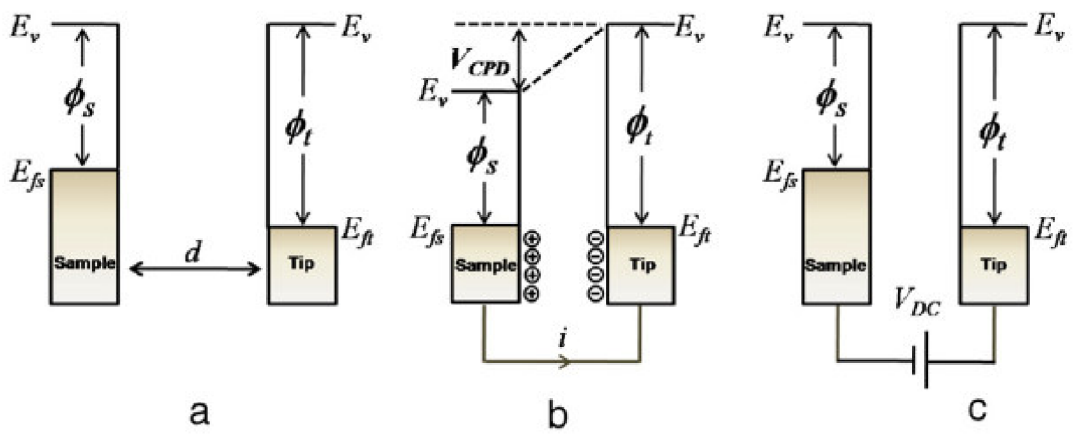

Fig. 1.6: Three cases of electronic energy levels when the tip and sample are separated by distance d: a) tip and sample have no electrical contact, b) tip and sample are in electrical contact, c) CPD nullified by an external bias voltage (V_{DC}). E_v is the vacuum energy level, E_{fs} and E_{ft} are the Fermi energy levels of the sample and the tip, respectively.

In Fig. 1.6 a): the Fermi energy levels are depicted, when the sample and tip are separated by distance d. Equilibrium in energy levels is achieved when the sample and tip are brought into conductive contact. This can be observed in Fig. 1.6 b), where due to the current flow, the Fermi levels equalize. Here, the tip and the sample surface are charged and an apparent V_{CPD} forms (although the Fermi levels are aligned, the vacuum energy levels are not). The electrical force generated by the V_{CPD} can be nullified by an external bias voltage (V_{DC}), which would have the same magnitude as V_{CPD} and opposite direction. Since the bias voltage (V_{DC}) is equal to the contact potential difference between the sample and the tip and the work function of the tip is known, the the work function of the sample can be calculated [23].

For the actual measurement of KPFM, an AC voltage (V_{AC}) and a DC voltage (V_{DC}) is applied to the AFM tip [24]. Oscillating electrical forces (from CPD) are generated between the sample and the tip by the V_{AC}, which are nullified by setting the V_{DC}. The electrostatic force (F_{es}) is given by:

$$F_{es}(z) = -\frac{1}{2}\Delta V^2 \frac{\partial C(z)}{\partial z}, \tag{1.7}$$

where z is the direction normal to the sample surface, $\partial C/\partial z$ is the gradient of capacitance between the tip and sample surface and ΔV is the potential difference between V_{CPD} and the voltage applied to the AFM tip. When V_{AC}, written as $V_{ac}\sin(\omega t)$, and V_{DC} is applied to the AFM tip, the voltage difference ΔV will be:

$$\Delta V = V_{tip} \pm V_{CPD} = (V_{DC} \pm V_{CPD}) + V_{ac}\sin(\omega t), \tag{1.8}$$

where the $\pm$ sign depends on where the bias voltage is applied, the sample (+), or the tip (-). The electrostatic force can then be written as:

$$F_{es}(z) = -\frac{1}{2}\frac{\partial C(z)}{\partial z}[(V_{DC} \pm V_{CPD}) + V_{ac}\sin(\omega t)]^2, \tag{1.9}$$

which can be divided into three separate parts:

$$F_{DC} = -\frac{\partial C(z)}{\partial z}\left[\frac{1}{2}(V_{DC} \pm V_{CPD})^2\right] \tag{1.10}$$

$$F_{\omega} = -\frac{\partial C(z)}{\partial z}(V_{DC} \pm V_{CPD})V_{ac}\sin(\omega t) \tag{1.11}$$

$$F_{2\omega} = \frac{\partial C(z)}{\partial z}\frac{1}{4}V_{ac}^2[\cos(2\omega t) - 1]. \tag{1.12}$$

F_{DC} causes a static deflection of the AFM cantilever, whereas F_{ω} is used to measure the V_{CPD} and $F_{2\omega}$ could be used for measuring local capacitance of the sample (capacitance microscopy). By using a lock-in amplifier, for getting the oscillating at frequency ω and feed-back loops, the value of V_{DC} is set so that F_{ω} equals to zero,

which is valid for $V_{DC} = \mp V_{CPD}$. With the acquisition of F_{DC} at every point of the selected area at a predetermined resolution of the sample surface, a map of the work function or surface potential is composed.

It is important to state however, that Eq. (1.7) only applies to measuring CPD on metallic samples. When it comes to semiconductors, space-charge-layer (SCL) has to be considered into the calculations. SCL on the surface of a semiconductor is well known. In this case, F_ω can be derived as:

$$F_\omega = -\frac{Q_s}{\epsilon_0} \frac{C_I C_D}{C_I + C_D} V_{ac} \sin(\omega t), \tag{1.13}$$

where Q_s is the total charge near the surface of the semiconductor, ϵ_0 is the dielectric constant, C_I is the capacitance associated with V_{ac} and the air gap between the sample and the tip, whereas C_D is the capacitance associated with V_{ac} and SCL in the semiconductor. The measured SPD of a semiconductor differs from the work function of a semiconducting material, because of the SCL near the surface.

2 Research

In this chapter, we will be looking into the transport properties of intrinsic CVD graphene, the various methods of lithography on graphene by AFM, lithographies on graphene without the use of an AFM and possibilities of using patterned nanostructures made of graphene.

2.1 Graphene mobility

Graphene as a material has proven itself to be capable of being a viable candidate for sensors of a large variety of chemicals [25]. However, the unique properties of graphene are typically best preserved in exfoliated graphene. On the other hand, the exfoliation method is not suitable for large scale fabrication of graphene based devices due to their limited area [26]. One of the most important properties of graphene, with regards to functionality of graphene based electrical devices, is its charge carrier mobility (or simply mobility) [27] [28].

Kumari et al. [29] used commercially available CVD grown graphene on copper foil (with a 95% purity) for measuring its electronic properties. After they confirmed the presence of single layer graphene with Raman spectroscopy, they used electron beam lithography (EBL) to form a Hall-bar structure for further analysis. The Hall-bar's main conductive channel was 5 µm in length and 2 µm in width. With these samples, they obtained the results observable in Fig. (2.1).

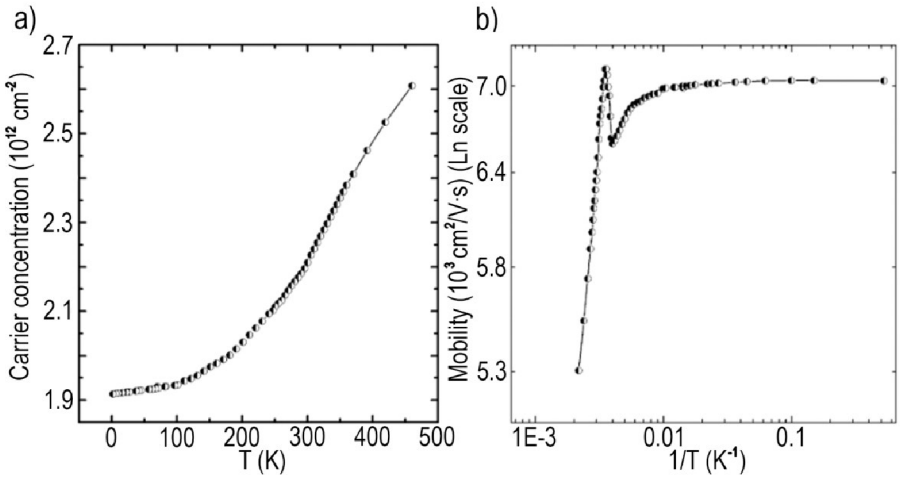

Fig. 2.1: Measurements done on a Hall-bar structure, a) depicts the carrier concentration with respect to temperature and b) depicts the dependence of mobility on the inverse of temperature. Adapted from [29].

In the end, they found that at temperatures below 100 K the charge carriers do not have enough energy to overcome grain boundaries (one dimensional defects in graphene), however, the above 100 K they do, which results in an increase in mobility. Above 290 K, the mobility diminishes with rising temperatures due to the increase in long range phonon scattering.

Chen et. al. [30] on the other hand, used exfoliated graphene from Kish graphite. Their initial goal was to find out if resistivity due to white-noise disorder or phonons depends on carrier density, n. They concluded that there is indeed a dependence and that it contributes only 30 Ω to the graphene's resistivity at room temperature (306 K). They also concluded that at low and room temperatures, the limitations of high graphene mobility are caused by charged impurities on the SiO_2 substrate, which they used. With this knowledge, they proposed that the mobility could reach up to $4 \times 10^4\,\mathrm{cm^2\,V^{-1}\,s^{-1}}$, which is comparable to the best field effect transistors (FETs).

Bolotin et. al. [31] avoided the interference from substrates by suspending their graphene. The devices used for measurements were fabricated by pressing a mechanically exfoliated graphene flake onto an SiO_2/Si substrate, lithographically patterning gold electrodes and subsequently etching away the SiO_2 under the flake. This resulted in the suspension of graphene ∼150 nm above the substrate. The goal of the study was to measure the conductivity of suspended graphene in a temperature range of $\mathrm{T} = 5 - 240\,\mathrm{K}$. The mobility measured at near-room temperature ($\mathrm{T} = 240\,\mathrm{K}$) was $1.2 \times 10^5\,\mathrm{cm^2\,V^{-1}\,s^{-1}}$, which indicated weak electron-phonon scattering. They concluded that the mobility of graphene is heavily dependent on extrinsic phonon scattering.

2.2 Lithography on graphene

In order to shape graphene into nano-electronic devices, one must first shape it in a controlled manner. This can be done in multitudes of ways, such as: photolithography, electron beam lithography, or even by using an atomic force microscope (AFM).

2.2.1 Lithography by AFM

The AFM platform offers a number of options for nano-lithography, whether it is on graphene or other materials. There are essentially three main methods, which we will be focusing on: mechanical lithography, local anodic oxidation and hydrogenation.

Mechanical lithography

This method essentially revolves around using the tip of the AFM probe to scratch away material from the sample surface (for instance, graphene). The usage of a highly durable material probe coating (such as diamond) is necessary for roughly retaining the dimensions of the tip. Finding the appropriate amount of compressive force is essential for the technique in order to plow away material.

Konečný et. al. [32] used mechanical lithography to separate an island of graphene from the rest of the grounded sample material. The goal of the study was to observe the charge propagation after the isolated graphene island was charged by an electrically biased AFM tip. Subsequently, Kelvin probe force microscopy (KPFM) was used to observe the propagation in time and under different relative humidities (RH). As such, the isolating capabilities of the method were thoroughly tested. The resulting resistivity was calculated to be between $1.2 \times 10^7\,\Omega$ (RH 65%) and $5.4 \times 10^{10}\,\Omega$ (RH 5%).

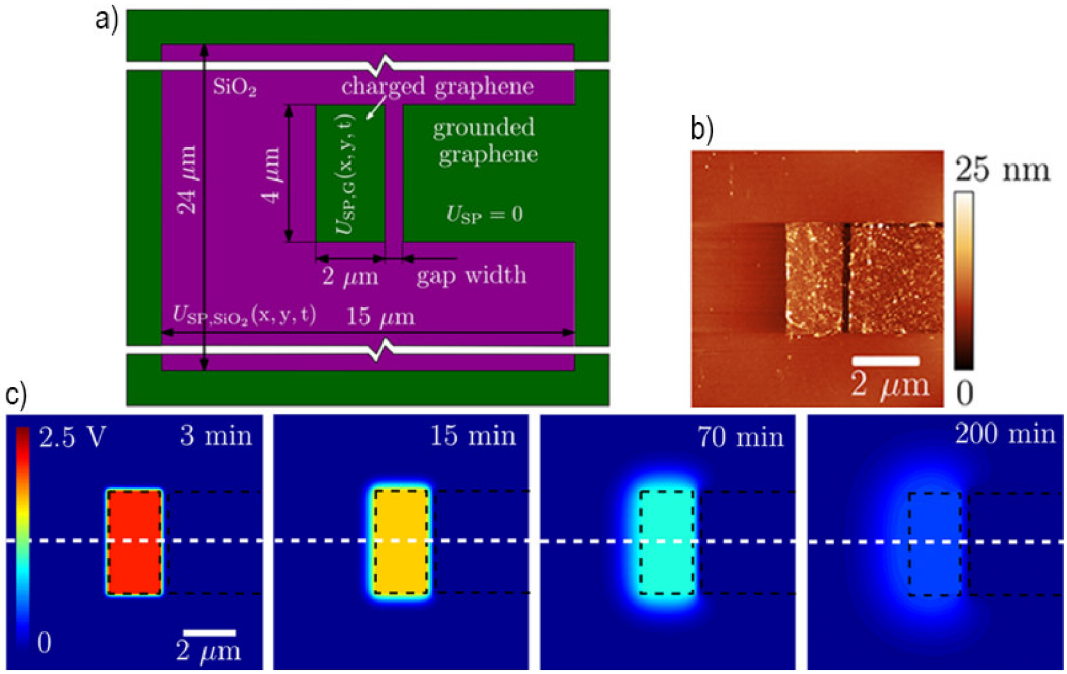

Fig. 2.2: a) Schematic illustration of the sample's geometry, b) an isolated graphene sheet from the grounded graphene by a gap, c) KPFM images scanned in different time frames, where the black dashed lines indicate the borders of the graphene sheets. Adpated from [32].

Vasić et. al. [33] approached the problem of mechanical lithography by using the tapping mode of their AFM instead of contact mode. They used low amplitudes of oscillations in order to hook into the graphene samples, which were able to cut the

graphene in the direction of probe propagation. Using this technique, the resulting carbon debris was greatly reduced. They called this method dynamic plowing, in contrast to static plowing (scratching). Deformation, which caused local strain on graphene, was also demonstrated, which opens up possibilities of tensile strength measurements of graphene. The resolution of their lithography was limited by the apex radius of the probe tips they used (DCP-20, diamond coated probes), which they concluded as improvable by the usage of thinner tips. They also proposed the usage of tip-enhanced Raman spectroscopy for strain measurements of graphene trenches.

Kun et. al. [34] aimed to improve the graphene edge quality at the sites of mechanical lithography. They did this by finding the crystallographic orientation of their exfoliated graphene crystal and adjusting the direction of plowing appropriately. Another one of their findings was the fact that beyond 1.5 nm of indentation, the chance of rupturing the graphene lattice dramatically increases. Quantum point contacts were also attempted by simply cutting two lines with one end coming in close proximity to the end of the other line, all the while the other ends of the lines reach the edges of the graphene flake. This way, they formed a 10 nm bridge between two large graphene areas.

Local anodic oxidation

The second method using an AFM as a lithography platform is local anodic oxidation (LAO), which requires higher than laboratory standard relative humidities (RH) around the AFM scanning head. Such values of RH can be achieved with the usage of a humidity chamber or custom-built environments. The other two requirements are: a conductive, grounded sample and a conductive probe tip [14].

Giesbers et. al. [35] attempted LAO on multi-layer graphene (graphite) at an RH of 55%, at room temperature and with a high bias voltage for oxidation ($|V_{ox}| = 25\,V$) between the tip and the sample. In their experience, it seemed impossible to oxidize the graphene layers if the procedure was to be done in the bulk of the sample, only managing to oxidize their layers when they started the experiments from the edges of the graphene layers. They reported on being able to form oxidized grooves as thin as 30 nm. Other than oxidation, they also attempted to peel off individual graphene layers from the samples by simply hooking their AFM tip into the sample's edge and dragging the probe across the sample in contact mode. This way, the upper layer(s) of graphene would be peeled off from the the bottom layer(s). They theorized that this technique opens up new possibilities of creating single-layer graphene sheets on GaAs as a substrate.

Weng et. al. [36] tried modulating the oxidation of graphene with LAO by using

different bias voltages on their AFM tip. The used voltage range was $15 - 30\,\mathrm{V}$ in a controlled humidity environment. Their attempts were done on exfoliated graphene sourced from HOPG and reported being able to form grooves down to $\sim$25 nm. They state that the oxidized graphene areas exhibit a bumpy topographic character at lower bias voltages, whereas they report trenches under higher voltages. The bumps (Fig. 2.3) are attributed to partial oxidation, where the oxygen incorporates into the graphene lattice, while the trenches are considered fully oxidized, where the carbon atoms form CO and CO_2 together with oxygen. In addition, they remarked that unlike previous experiments in the field, oxidizing the bulk of the material did not pose a challenge and that they were able to demonstrate the technique both on the edges and the bulk.

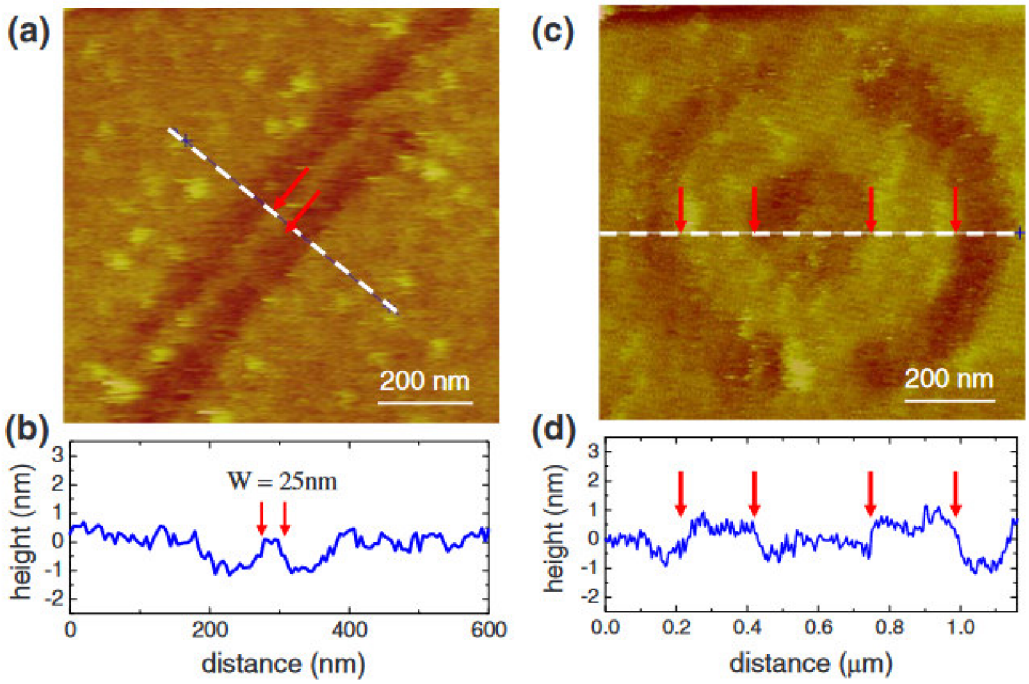

Fig. 2.3: a) AFM image of nanoribbons with width and length of 25 and 800 nm. b) surface profile along the dashed line in a). c) AFM image of nanorings (inner and outer radius of 160 and 380 nm, respectively). d) surface profile along the dashed line in c). Available from: [36].

Masubuchi et. al. [37] took interest in band gap engineering possibilities in the form of graphene nanoribbons (GNRs) and the transport phenomenon of the half-integer quantum Hall effect. They obtained their graphene from Kish graphite and used a heavily doped Si wafer as a substrate, which they also used as a global back gate. For LAO purposes, the RH was kept in a range of $39\% - 44\%$ and a positive bias voltage was applied to the substrate (instead of the tip, in contrast to other

studies) at 35 V. They used these parameters on single-layer, bilayer and multilayer graphene, whereby the number of layers was confirmed by measuring the quantum Hall effect and using Raman spectroscopy. The grooves they managed to form can be seen in Fig. (2.4).

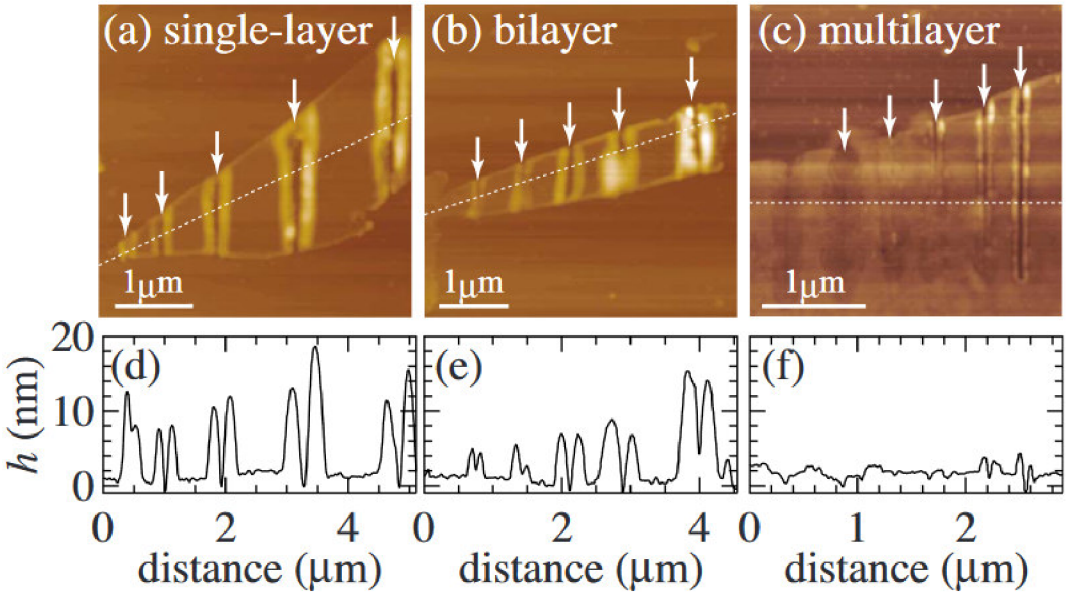

Fig. 2.4: AFM images of (a) single-layer, (b) bilayer and (c) multilayer graphene flakes, where the arrows mark the direction of LAO lithography with speeds $v_s = 160, 80, 60, 40, 20$ and $10\,\mathrm{nm/s}$ (from left to right). (d), (e) and (f) depict the topography of the samples along the segmented white lines in (a), (b) and (c), respectively. Adapted from [37].

Neubeck et. al. [38] carried out experiments with LAO on graphene under different RH values, while noting that oxidation above 80% did not occur. Their findings stated that the most reliable combination of tip bias voltage and RH was $-7\,\mathrm{V}$ in an RH of 70%, while remarking that with lower RH (such as 70%) they needed significantly higher bias voltages (upwards of $-20\,\mathrm{V}$). After these experiments, they tried to fabricate nanoelectronic devices, namely a quantum point contact as an example. With this goal in mind, they managed to oxidize lines into their graphene flake, obtaining an unaffected graphene constriction with an area of $60\,\mathrm{nm} \times 60\,\mathrm{nm}$. They also investigated the behaviour of graphene in its bulk form (HOPG) by carrying out LAO on one. Although, they concluded that their comparison of oxidation between graphene and HOPG is not suitable for making generalized statements.

Puddy et. al. [39] investigated the differences between cuts and pseudocuts on graphene. The cuts in this study refer to lasting lithography by LAO, whereas pseudocuts refer to locally charged areas by the AFM tip that did not manage

to electrochemically alter the graphene layer. They used mechanically exfoliated graphene on an SiO_2/Si substrate. In their experiments, the RH was unchanged and kept at 50%. They oxidized their graphene samples with different bias voltages and found that the threshold for oxidation varied from $\sim -3.5\,\mathrm{V}$ to $\sim -5\,\mathrm{V}$. In the end, they managed to form islands of graphene in the shape of triangles by three lines made with LAO, which were characterized by scanning electron microscopy (SEM), where the cuts (non-conductive islands) and pseudocuts (conductive islands) were easily distinguished. The tip currents in Fig. (2.5) according to the study drop to $\sim 0\,\mu\mathrm{A}$ during LAO.

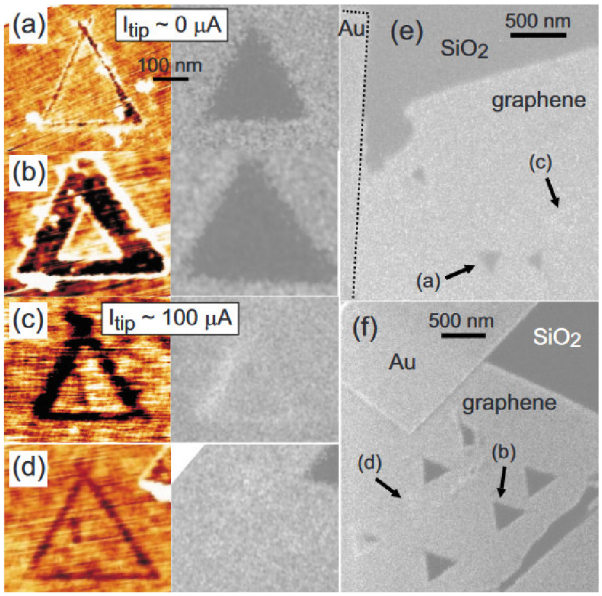

Fig. 2.5: [(a) and (b)] AFM (left) and SEM images (right) of two triangles cut with $|V_{bias}| > |V_{thresh}|$ such that the tip current, $I_{tip} \sim 0$ during cutting. [(c) and (d)] AFM (left) and SEM images (right) of two triangles cut with $|V_{bias}| < |V_{thresh}|$ such that the tip current, $I_{tip} \sim 100\,\mu\mathrm{A}$ during cutting. [(e) and (f)] SEM images of the areas of graphene where the triangles were cut, with the arrows indicating the location of the triangles shown in panels [(a)−(d)] Adapted from [39].

Byun et. al. [40] attempted both hydrogenation and oxidation of monolayer graphene for lithography purposes. For hydrogenation, the bias voltage is opposite compared to LAO. They confirmed the presence of either hydrogenated or oxidized graphene by micro-Raman spectroscopy. In an effort to maximize the resolution of LAO, they lowered their initial RH (33%) to 20%, where they stated that the threshold bias voltage was $|V_{bias}| = 4.5\,\mathrm{V}$.

Masubuchi et. al. [41] experimented with the fabrication of graphene/graphene oxide/graphene (G/GO/G) junctions with different GO strip widths. Single-layer

graphene flakes were deposited on a SiO_2 substrate, where the graphene was connected by metal electrodes on opposite sides of the flake. The GO strip width was influenced by changing the bias voltage on the tip. When the $|V_{bias}|$ was increased from 5.5 to 9 V, the width also increased from 20 to 50 nm. By using a back gate on the bottom, heavily doped, Si substrate below the SiO_2, they were able to measure the minimum conductance (G_{min}) of their samples after LAO strips were formed. They reported that as the $|V_{bias}|$ increased, the G_{min} decreased, providing possibilities for conductance tuning of such junctions.

Lee et. al. [42] aimed to create graphene systems of chips (SoC) with LAO. The SoC would be made of G/GO/G junctions, which could serve as transistors or as memory elements. The difference between the two systems would be extent of oxidation, as the GO element would be formed with different $|V_{bias}|$. GO made with $|V_{bias}| = 7\,V$ results in a barrier that exhibits Fowler-Nordheim tunneling, which causes the graphene to have a large modulation of of graphene's Fermi level. Whereas GO made with $|V_{bias}| = 9\,V$ exhibits non-volatile resistive switching.

2.2.2 Other lithography techniques

Although techniques using an AFM seem to be ideal for certain applications, it remains to be a very slow approach with advantages that are not prioritized in most cases. For general lithography purposes of graphene, other, faster methods are preferred, such as: photolithography and electron beam lithography (EBL).

Electron beam lithography

This method requires a number of steps, which will be better detailed in the experimental chapter of this thesis. However, for the intents and purposes of this section, we will mention and recognize that the method requires the usage of resists, wet-transfer, development and the operation of an SEM.

Gardener et. al. [43] used ice-assisted EBL on graphene, which acts as a resist for the graphene layer. The experiment was conducted on both CVD and exfoliated graphene with an SiO_2/Si substrate. The samples were cooled to $\sim -165\,°C$ in a custom-built, field emission SEM. A $100 - 200\,nm$ thick amorphous ice layer was vapor deposited onto the sample surface, which was then e-beam dosed in the selected region. The ice was removed using sublimation at $-100\,°C$, then warmed to room temperature and removed from the vacuum environment. Raman spectroscopy measurements indicate that the graphene in the areas exposed to the e-beam was removed completely. This modified EBL technique removes the need for polymer-based resists, which could leave residues behind on the samples.

Sommer et. al. [44] recognized the difficulty of fabrication of suspended graphene based nanoelectronic devices. They managed to form such structures by shaping Au contacts with EBL on graphene on an SiO_2/Si substrate and selectively etching away a SiO_2 layer with hydrofluoric acid. The suspended graphene was finally etched with gas-assisted electron beam (FEB), which used a carbon etch gas injection system. The achieved resolution with this setup was $\sim$7 nm.

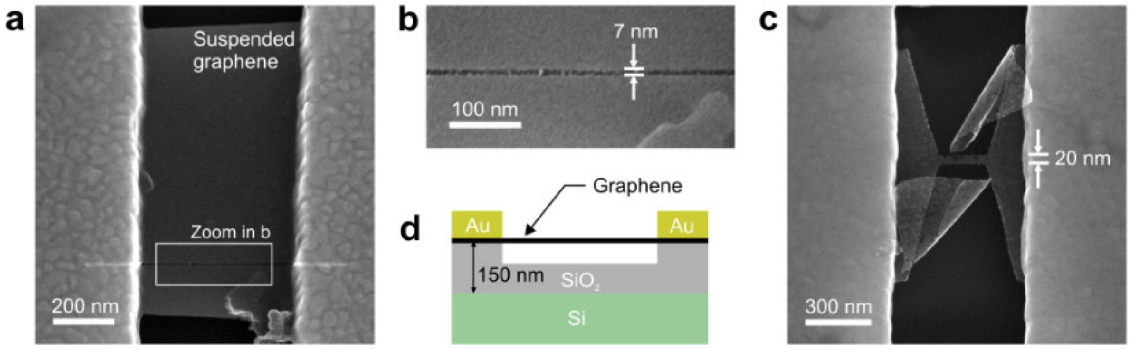

Fig. 2.6: Nano-etched suspended graphene: (a) SEM image of suspended graphene cut by e-beam-induced etching. Two Au contacts separated by 500 nm were placed and by the removal of SiO_2, the graphene was suspended. (b) zoom-in of the line-cut by FEB with a feature size of $\sim$ 7 nm. (c) SEM image of a suspended graphene nanoribbon with a width of 20 nm (with rolled-up grapheneon the sides). (d) schematic picture of the sample structure. Adapted from [44].

Fan et. al. [45] found that during Raman spectroscopy of standard electron beam lithography and photolithography, the persistence of resists can be detected as contaminations of graphene. The research concluded with the finding that the polymer resists, such as electron-sensistive polymethyl methacrylate (PMMA) resist residues, can be removed by annealing the sample at 300 °C. However, the same cannot be said about the AZ6624 photo-sensitive resist, which remains on the graphene layer even after the previously mentioned annealing process. These disorders can influence the electronic capabilities of the material, which are often taken for granted. As such, the order of steps taken during graphene lithography processes have to be evaluated.

Photolithography

This type of lithography, like EBL, under standard circumstances involves the exposure of the samples, spin-coated with a positive or negative resist, to a beam of photons. The wavelength of the electromagnetic waves is usually in the ultra-violet

(UV) range. For positive resists, the exposed areas are etched away with the development chemical, or for negative resists, the unexposed areas. Finally, the residual resist is removed with a different chemical.

Venugopal et. al. [46] measured the transport properties of graphene field effect transistors with respect to temperature change. They used HOPG sourced graphene flakes on an SiO_2/Si substrate. Photolithography was used for placing Au contacts with a positive resist and a Cr mask to protect the graphene from the UV beam. The process was finished with the removal of the remaining resist with the Cr layer.

Shi et. al. [47] aimed to increase the success chance of graphene based device fabrication by optimization of the process. Their steps include photolithography for patterning the Au electrodes for their devices and for the patterning of the graphene channel for functionalization. Although, their technique involves the usage of PMMA, with the modification to standard procedures by a so called "bubbling transfer" on Pt foil, they were able to produce devices, in terms of transport properties, similar to structures made with EBL. The resulting yield percentage of operational devices was 86% (70 out of 81 samples).

Choi et. al [48] came up with a new photolithography process, which supposedly solves the polymer resist residue issue. By introducing a buffer layer between the graphene and the resist, the resulting samples had no major detectable resist residues. The buffer layer, surfactant and solvent were solutions of AZ nLOF 2035 photoresist (LOF, Merck), propylene glycol monomethyl ether acetate (PGMEA, $> 99.5\%$, Sigma Aldrich) and sodium dodecyl sulfate (SDS, 85.0%, Samchun), respectively. The mechanism of the resist's and the buffer's removal were examined with DFT calculations and XRR studies. The resulting graphene was reported as having superior quality over the graphene patterned using the standard method, which does not involve a buffer layer.

2.2.3 Graphene based sensors

The resistance in graphene is at its highest point at what is called the Fermi level. In intrinsic (undoped) graphene, this point has the lowest amount of states for electrons. Whenever a molecule on the surface of graphene influences the transport properties, the Fermi level shifts, which can be detected as a decrease in resistance. With this property in mind, many studies have tried fabricating detection devices using graphene [49]. When graphene is shaped into the field effect transistor (FET) configuration, the Fermi level can be artificially adjusted with the application of a gate voltage [50] [51]. This allows potential sensing devices to be calibrated and configured [52].

Chen et. al. [53] tested the capabilities of O_2 detection by a graphene based

sensor. They used CVD graphene, where they selected a region of 1 cm × 1 cm, where the graphene was uniform enough for their experiment, which was then placed on an SiO_2/Si substrate. By using a gas isolating chamber filled with N_2 and controlled doses of O_2, the Ohmic contacts of the detection system were able to determine the change in resistance when a constant bias voltage (500 mV) was applied to the sample. The detection limit of their system was determined to be 1.25% in volume ratio.

Dan et. al. [54] set out to explore the intrinsic properties of graphene after removing contaminations from the material. They found that the EBL processing of samples leaves the graphene layer covered in a $\sim$1 nm thick layer of contaminants, which was roughly removed by their cleaning procedure. The samples were cleaned by heating them in a flowing H_2/Ar (850 sccm Ar, 850 sccm H_2) at 400 °C. This procedure reduced the contaminants to roughly one third of its original quantity. Cleaning of samples in this fashion was deemed necessary for chemical functionalization of graphene sensors for achieving lower detection limits.

Borini et. al. [55] developed ultrafast graphene oxide based sensors of moisture. They deposited GO elements at various thicknesses and found that when it was decreased to 15 nm, the response and recovery time of the sensing capability reduced to 30 ms. This allows the technology to be used for detecting the moisture content of a user's breath and opens up the possibility of detection of other chemicals at a high refresh rate.

Yoon et. al. [56] reported on a graphene based CO_2 gas sensor, where the graphene layer was made by mechanical cleavage. The graphene sensor showed significant changes in its conductance depending on the different concentrations of CO_2 in air. The response time of the device was less than 10 s, opening up possibilities for environmental monitoring.

3 Thesis results and experimental setup

After providing the theoretical background and research on the topic at hand, this chapter will provide a summary of the fabrication process, the experimental setup for measurements, the achieved results and the various challenges encountered during the experiments. We will also be mentioning the practice phase of the project and its significance.

3.1 Sample fabrication and preparation

For the exploration of AFM based lithography possibilities on graphene, one must have access to suitable samples on which such techniques can be tested. However, the graphene layer has to be of high quality, while covering a large enough area, where nanoelectronic devices can be fabricated, such as Hall probes. This device, in its FET form, was selected due to its ability to provide information on its change of resistance, when lithographic modification takes place on its surface. As such, CVD graphene was picked for our intents and purposes. The description of the devices' fabrication is of high importance, due to the process's complexity and better understanding of its geometry. All Hall probe samples in this chapter were fabricated by Bc. Linda Supalová.

The samples, which were provided, were designed to have a global back gate. This back gate was not utilized during our measurements. However, it serves as an explanation for the usage of the given graphene carrying material, which was a 285 nm thick SiO_2 layer on top of an Si substrate. The thickness of the SiO_2 was selected based on its optical properties, which allows the graphene layer to be seen with optical microscopy.

In the first step of Hall bar fabrication, the lower electrodes are made, which come directly in contact with the graphene layer by the end. These contacts are comprised of a 5 nm thick Ti adhesive layer and a 25 nm thick Au layer. Secondly, these lower electrodes then connect to the higher electrodes, comprised of the adhesive 5 nm thick Ti layer once more and a 100 nm thick Au layer. The taller electrodes are on the end connected by wire bonding to plugs on the the chip expander, allowing the sample to be connected to measuring devices and current sources.

The process was optimized by the usage of lithographic masks for both steps. This meant that the several chips could be made at once instead of the standard direct-write methods, which would be time consuming an resource inefficient. The chips themselves had an area of 7×7 mm which were arranged in a 6×6 grid on the SiO_2/Si. Prior to UV lithography, the SiO_2/Si substrate was cleaned by acetone, isopropyl alcohol (IPA) and oxygen plasma. Then the adhesion promoter (AR

300-80) and positive resist (AZ 701 MiR) were spin-coated on the substrate after which they were exposed in UV lithography and developed. Reactive-ion etching with oxygen plasma followed the process to clean the samples after mask development. The deposition of the Ti and Au layer were done by electron beam vapour depositioning, which filled the gaps in the mask. By a lift-off process, the unexposed resist with deposited material were removed. This process was done separately for the lower and the higher electrodes, both with their respective lithographic masks. The process can be observed in order in Fig. (3.1).

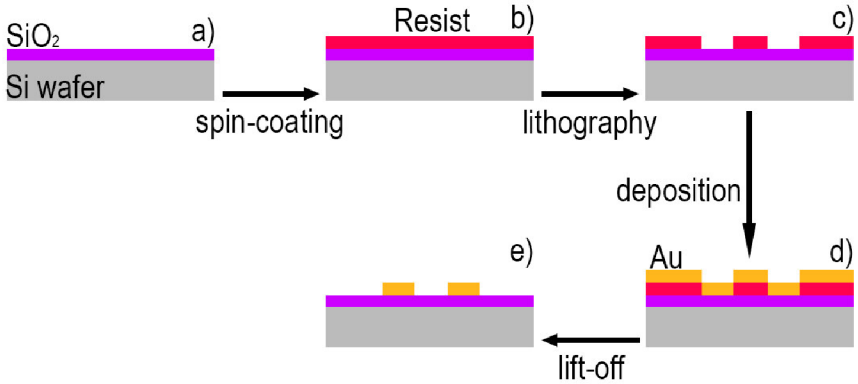

Fig. 3.1: Electrode formation by UV lithography: a) SiO_2/Si substrate. b) spin-coating of the resist. c) lithography involving exposure and development. d) deposition of the adhesive Ti layer and the Au layer. e) lift-off process.

In the next step, the graphene layer was transferred onto the prepared chips with the prepared electrodes. Before the transfer procedure, the individual chips are treated with acetone, IPA and oxygen plasma, followed by annealing at 180 °C for 45 minutes. During the project commercially bought CVD-grown graphene on copper foil on both sides (Fig. (3.2, a))) was used. Firstly, the graphene got spin-coated with polymethyl methacrylate (PMMA) on one side (Fig. (3.2, b))), while the other got cleaned of graphene by RIE (Fig. (3.2, c))). To reduce the amount of PMMA contamination of graphene, a thin layer of PMMA 50K was used with a thicker top layer of PMMA 950K. The copper foil was then etched away with $Fe(NO_3)_3 \cdot 9\,H_2O$ (Fig. (3.2, d))). The resulting graphene and PMMA layer was then cleaned in diluted HCl (Fig. (3.2, e))). The graphene with the PMMA was then moved to deionized water, together with the prepared chip, which is used as a scoop to pick up the graphene from the beaker (Fig. (3.2, f))). After the chips are taken out and dried, a drop of PMMA is then used to partially dissolve the supportive PMMA layer on the graphene (Fig. (3.2, g))). The residual PMMA is

then removed by acetone (Fig. (3.2, h))) and the chips are once more annealed at 180 °C for 15 minutes (Fig. (3.2, i))).

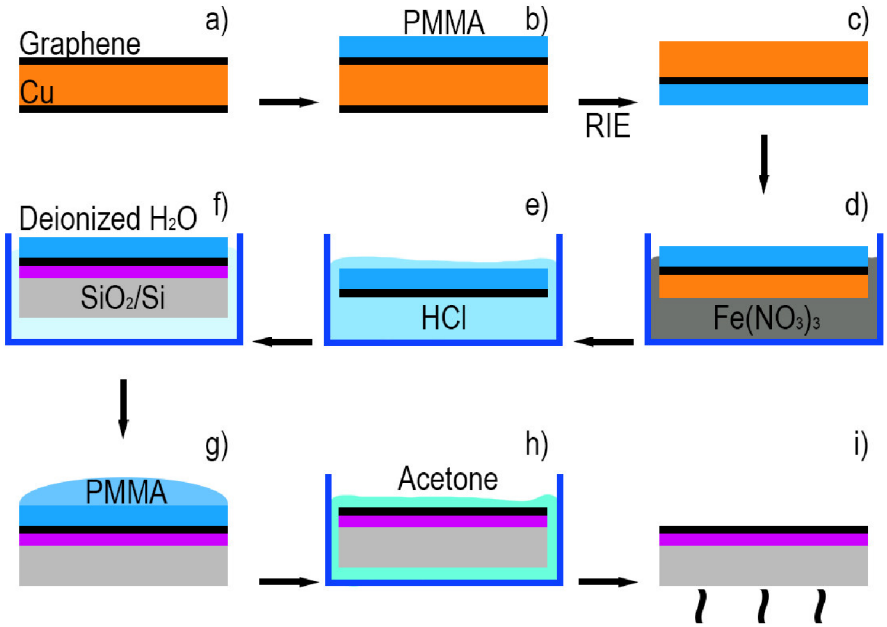

Fig. 3.2: Graphene wet transfer process: a) Cu foil with graphene on both sides. b) PMMA spin-coating on graphene from one side. c) reactive-ion etching of the opposite side. d) etching of Cu foil. e) cleaning with HCl. f) cleaning in deionized water with chip transfer. g) adding of PMMA droplet. h) chip cleaning with acetone. i) annealing of samples.

The next step in the Hall probe fabrication was the formation of the Hall bar shape from graphene. To combat certain issues, such as the graphene layer rolling up or forming tears, an extended patterning procedure was devised. In the first step, two resist layers were spin-coated onto the prepared samples (Fig. (3.3, a))), an e-beam resist (for electron beam lithography (EBL), such as CSAR or HSQ (hydrogen silsesquioxane)) and an optical resist (Fig. (3.3, b))). After exposure by UV lithography and photoresist development, the hardened photoresist remains where the Hall bar structures will be located (Fig. (3.3, c))). The remaining resist is removed with RIE and organic solvents (Fig. (3.3, d, e))). The second step in graphene formation starts with spin-coating e-beam resist onto the sample (Fig. (3.3, f))). It is then exposed by e-beam and developed (Fig. (3.3, g))). Finally, the graphene is removed by RIE and the remaining resist by organic solvents (Fig. (3.3, h))).

In the final steps, the prepared chips with the Hall bars are glued to a chip expander using a conductive silver paste and wire bonded to aluminum plugs. The

chip expander was then glued to a magnetic holder using carbon tape.

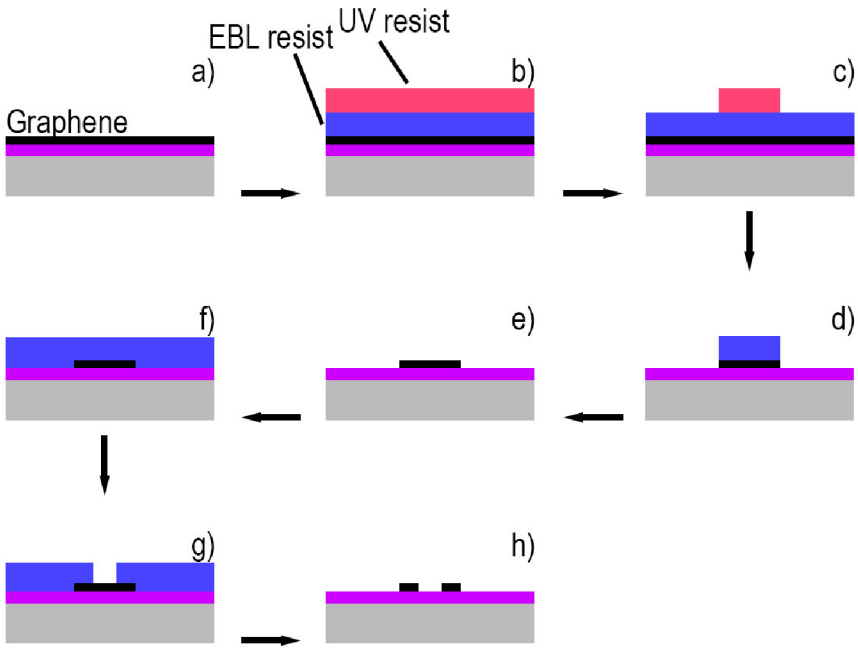

Fig. 3.3: Graphene formation into the Hall bar structure: a) prepared samples with transferred graphene. b) spin-coating of resists. c) photolithography of the sample. d) reactive-ion etching. e) resist removal. f) spin-coating of e-beam resist onto the chip and remaining graphene. g) exposure and development. h) final resist removal.

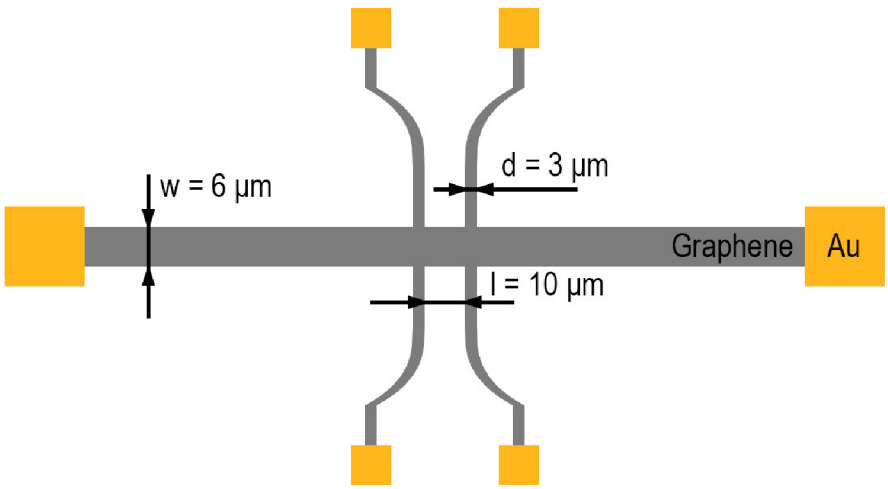

Fig. 3.4: Graphene hall bar geometry, where the thinner, side channels are used for measurements of potential difference and the thicker, main channel is used as a connection between the source and drain of electric current.

The final geometry of the Hall bar structure, which was used during measurements, can be observed in Fig. (3.4).

3.2 Experimental setup

For measuring the transport properties of our samples, we needed to set-up the necessary circuitry using a variety of devices, while incorporating the AFM platform for simultaneous measurement of transport and KPFM. The sample must also be suitable for LAO lithography in general.

For better understanding of the circuitry, the chip on its expander can be viewed in Fig. (3.5, a)). The Hall bar made of graphene can also be seen in the optical microscope image in Fig. (3.5, b)). Each chip contains three Hall bar structures, out of which two are connected to the plugs.

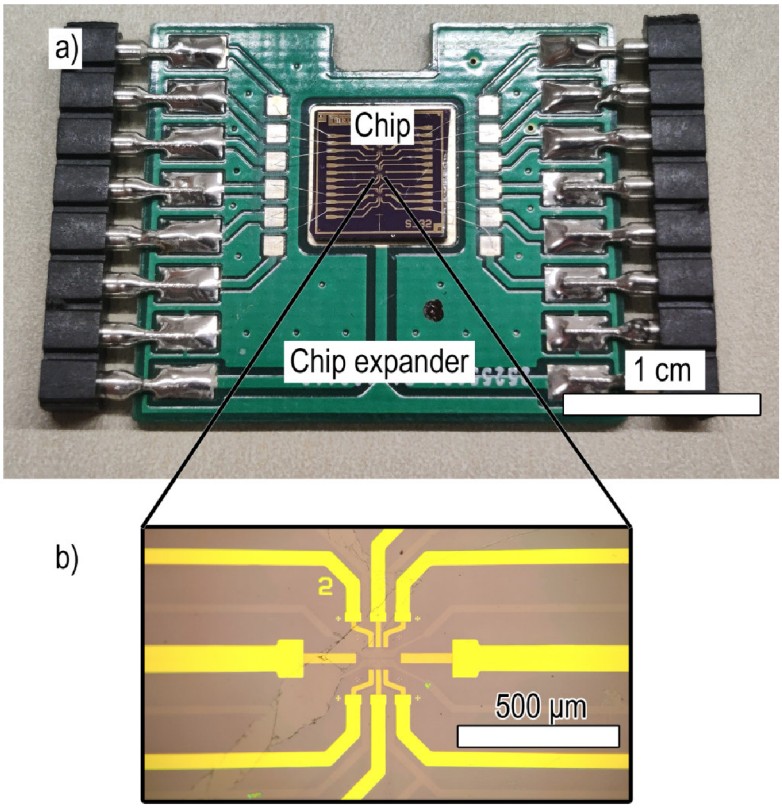

Fig. 3.5: Graphene Hall probe sample: a) picture of a sample chip, glued to its expander. b) image of the Hall bar geometry observed with an optical microscope.

The aluminum plugs (protected by black plastic) can be seen on the chip expander's left and right sides. The plugs themselves are used to connect the sample to a switch-box via micro-cabling. The switch-box (Fig. 3.6, c)) serves as a platform

for creating circuits between devices, adding additional resistances and grounding of individual connections. During the experiments, two direct current sources were connected to the sample, together with a nano-voltmeter and a PC acting as a control unit. The current source units were both Keithley model 2661's, while the nano-voltmeter was a Keithley model 2182A, all of which were connected to the PC. The software controlling the devices was an in-house programmed device managing software, which was set for a 4-point contact measurement. The circuit and the setup, which was used during the measurements, can be observed in Fig. (3.6, a)).

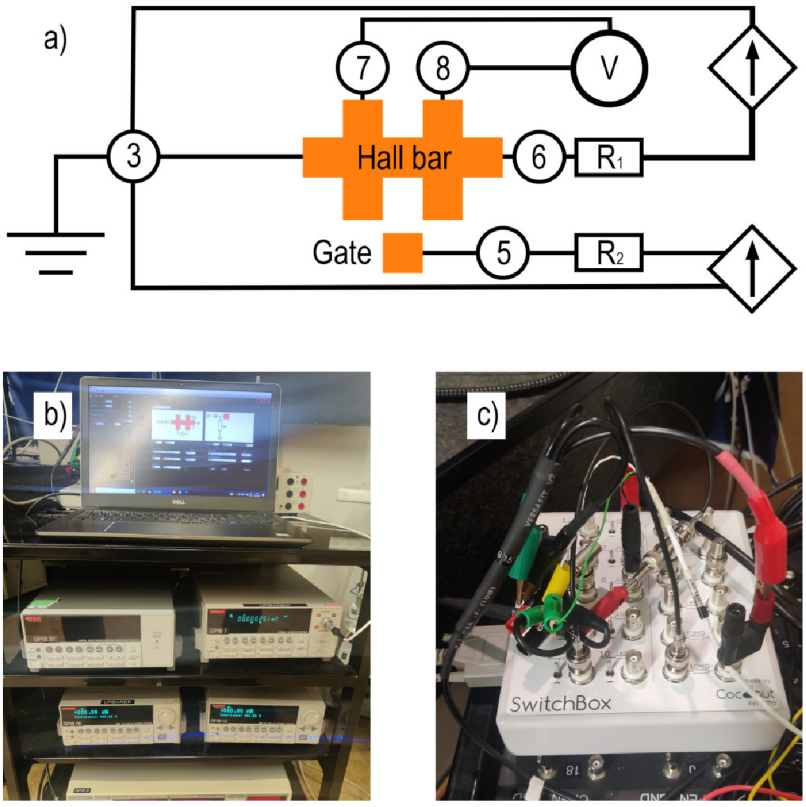

Fig. 3.6: Transport measurement setup: a) schematic representation of the transport measurement circuit. b) image of the measurement station with the used devices turned on. c) image of the switch-box utilizing the circuit from a).

Although the current source used for applying the gate voltage was set-up for potential usage, its main purpose was to remove any surplus charge from the substrate through grounding. Additional resistances were also applied to the circuit, namely R_1 was set to 10 MΩ and R_2 was set to 1 MΩ. The numbers seen in Fig. (3.6, a)) represent the plugs used on the switch-box, which represent the individual cables used to connect to the chip. Here, the cables which were functional at the time of measurement were the ones depicted in the schematic. For the setup of

the main current source (the current going through the main channel of the Hall bar) the auto-range was turned off and the compliance (maximum voltage used to attempt reaching the set current) was 1.2 V. As for the nano-voltmeter, the calculations were set to display the resistance instead of the voltage (calculated from the set current) and the frequency of data acquisition was set to 2 Hz (two measurements per second).

After setting up the cabling of the sample on the AFM base (Fig. 3.7, a)), the AFM probe was inserted into the AFM head for standard scanning procedure (Fig. 3.7, b)). As the cables are particularly sensitive to damage resulting from overt bending, proper cable management was an absolute necessity to make room for the humidity chamber (Fig. 3.7, c)). The chamber was a home-built device, which could be used to regulate the RH. We used dry nitrogen gas to lower the RH, while a bubbler was used to increase RH. The device was managed by a control software, similar to the one used for setting up the current sources and nano-voltmeter.

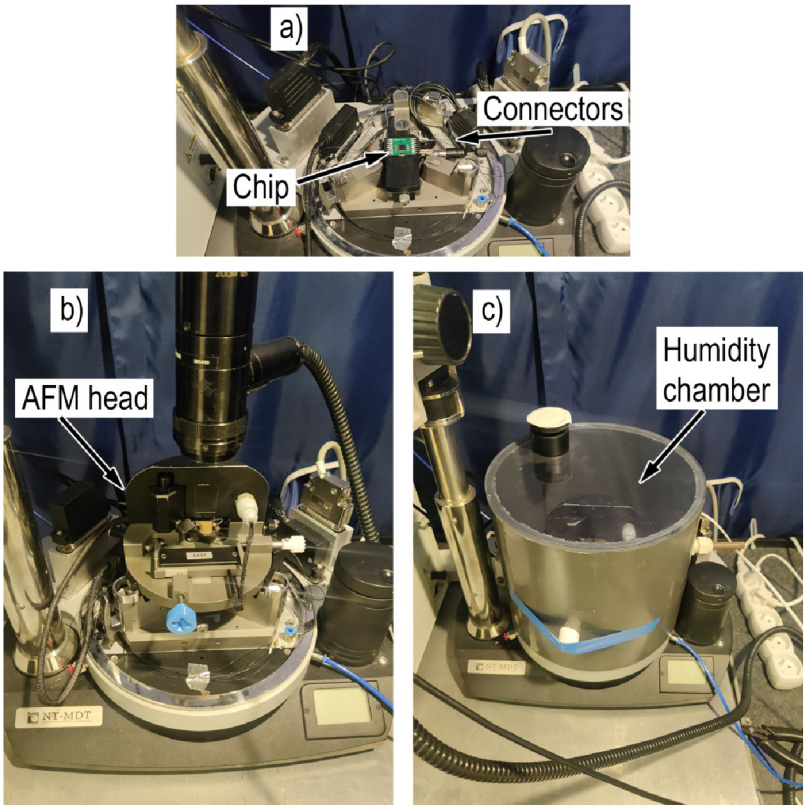

Fig. 3.7: a) image of the chip sample placed on the sample holder of the AFM with plugs attached to the chip expander. b) image of the AFM set to measure in ambient laboratory conditions (AFM by NT-MDT, model NTEGRA Prima). c) image of the AFM set to measure in controlled conditions.

3.3 Results

In this section, we will report on the successful attempts at completing the thesis goals and provide the used parameters for the acquisition of the data. Some undesired compromises, in terms of experiments, were a necessity, for reasons that will be specified in the section following the results.

3.3.1 Hall probe main channel interruption

Firstly, to measure the isolating capabilities of LAO, we planned on interrupting the sample by a simple line lithography, perpendicularly through the middle of the main channel of a Hall probe. Subsequently, add a second line next to it and observe the change in resistance.

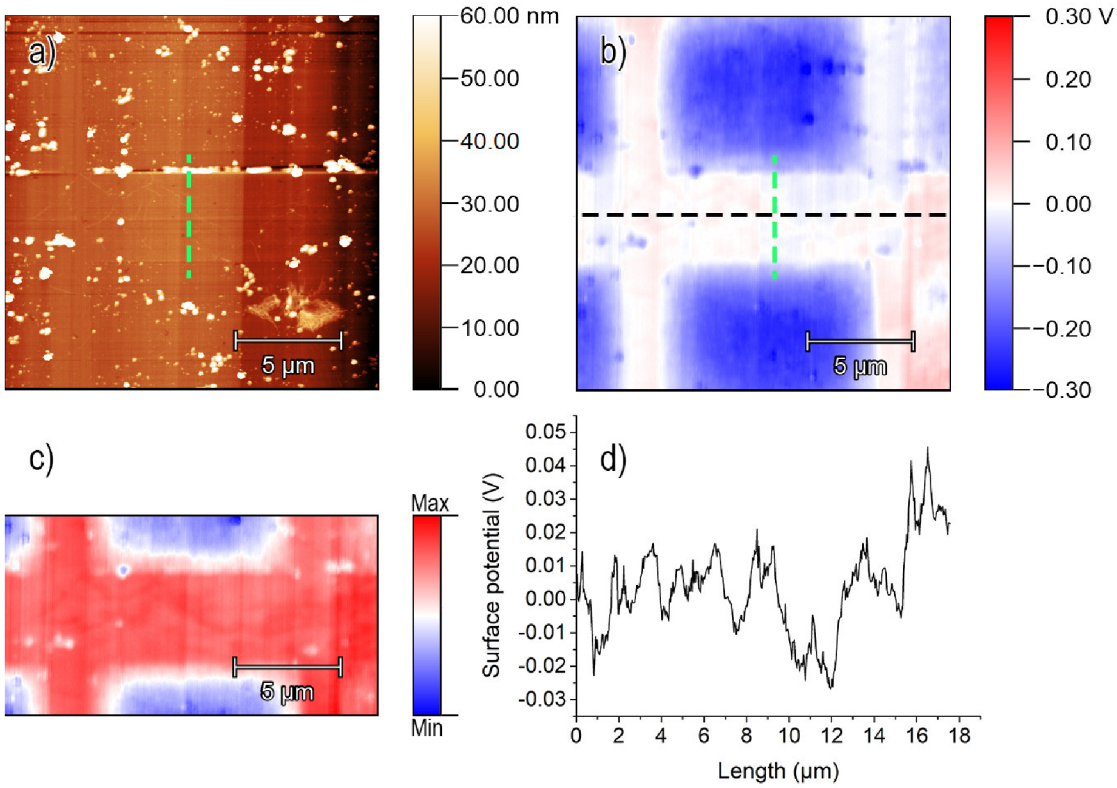

Fig. 3.8: Measurements before lithography: a) AFM topographic image of the sample Hall probe structure, where the green, segmented line represents the selection of area for the following LAO lithography. b) KPFM image, where the electric current flows from the right side of the main channel, to the left. c) High-contrast surface potential image of the middle part of the Hall probe main channel. d) Line profile of the surface potential taken from the black segmented line in image b).

Before any lithography was done, the sample's topography and its surface potential were measured simultaneously in semi-contact tapping mode and KPFM, which can be viewed in Fig. (3.8, a) and b), respectively). The high contrast image (Fig. (3.8), c)) is a re-scaled portion of the image depicting the surface potential, for better contrast and visibility of details. Probes used for these images were NSG10 - Au, oscillated at a set-point of 6.5 (65% of the free oscillation amplitude of the cantilever) with a feedback gain of 0.3 (responsiveness of the feedback system to changes in topography). The scanning area was originally $20 \times 20\,\mu m^2$, which consisted of 512×512 pixels. However, due to correctional distortions in post-processing, this was down-scaled to 450×450 pixels (equivalent to $17.58 \times 17.58\,\mu m$). The scanning speed for analysis was $20\,\mu m/s$ (0.5 Hz, which is one line scan per two seconds). All analytical measurements in this section were done at 3% RH.

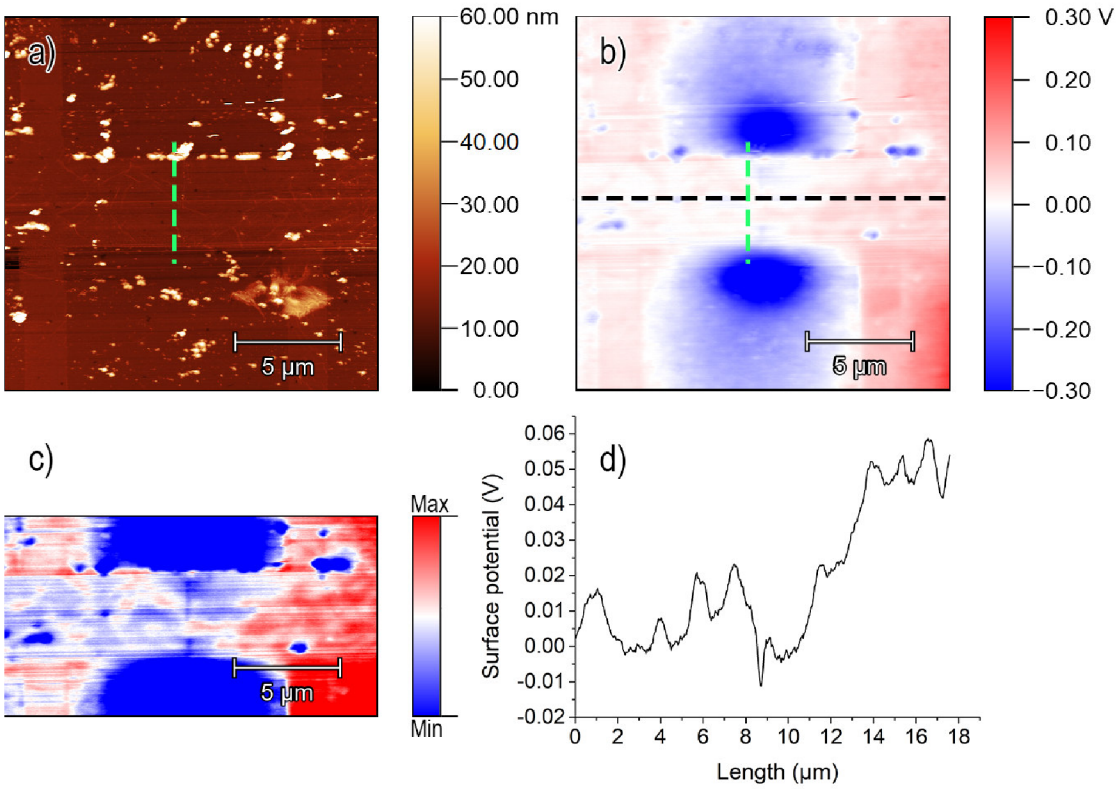

Fig. 3.9: Measurements after line lithography: a) AFM topographic image of the sample Hall probe structure, where the green, segmented line represents the second selection of area for the following LAO lithography. b) KPFM image, where the electric current flows from the right side of the main channel, to the left. c) High-contrast surface potential image of the middle part of the Hall probe main channel. d) Line profile of the surface potential taken from the black segmented line in image b).

In Fig. (3.9), we can observe the line lithography done by LAO, which was conducted under 55% RH, with a static bias voltage of $-8\,\mathrm{V}$. The lithography itself was done by switching the AFM probe to a DCP-20, diamond coated, nitrogen doped, non-contact probe. The area of interest was approached and the AFM was switched to contact mode, where the tip would be in contact with the sample's graphene surface during lithography at all times. As to not damage the sample surface, the lowest possible contact force was set.

For modifying the graphene with LAO, a scan was started with only two lines drawn under the conditions described above, at a speed of 200 nm/s. The images in Fig. (3.9) were acquired after exchanging the AFM tip to the previously used probe and the same conditions were applied during the scanning procedure. In Fig. (3.9, c)), thanks to the high contrast, we can observe the line's location and its shape. The global minimum of the graph depicted in Fig. (3.9, d)), at the site of the lithography, is further proof of its presence. We can also observe the local charging of the insulating SiO_2 layer at the end points of the line drawn by LAO.

In Fig. (3.9, a)), we can see that the topography of the graphene sheet did not suffer any major damage by the probe. The feedback gain in contact mode was only 0.2, which meant that the feedback system was less sensitive to rapid changes in height. Although, this is risky for the fact that the graphene may be damaged in case the feedback system does not correct its height in time, it also allows the tip of the probe to be as much in contact with the graphene layer as possible in case the tip encounters a contaminant fragment.

The simultaneous transport measurements also registered an increase in resistance. Throughout the experiments, a 100 nA current was flowing through the samples, while the voltage difference was measured by the nano-voltmeter. With these two pieces of information, the resistance was calculated automatically. The resistance before the line lithography was $(1660 \pm 20)\,\Omega$ and after the lithography was done, the resistance increased to $(2550 \pm 20)\,\Omega$.

After the scans for the analysis of the first lithography images were done, we aimed to add a second line next to it. The selected area can be observed in Fig. (3.9, a) and b)), marked by the green segmented line. The same parameters and procedures were used as in the first drawn line.

To increase the stability of the LAO lithography, we have decided to let the AFM do four scan lines instead of just the previous two. However, due to a system fault better described in the latter part of this chapter, the probe tip scratched a (23 ± 2) nm deep and (180 ± 10) nm wide nano-canyon into the sample. This was not intentional. Although, this did devalue further measurements and the sample as a whole, some information may still be salvageable.

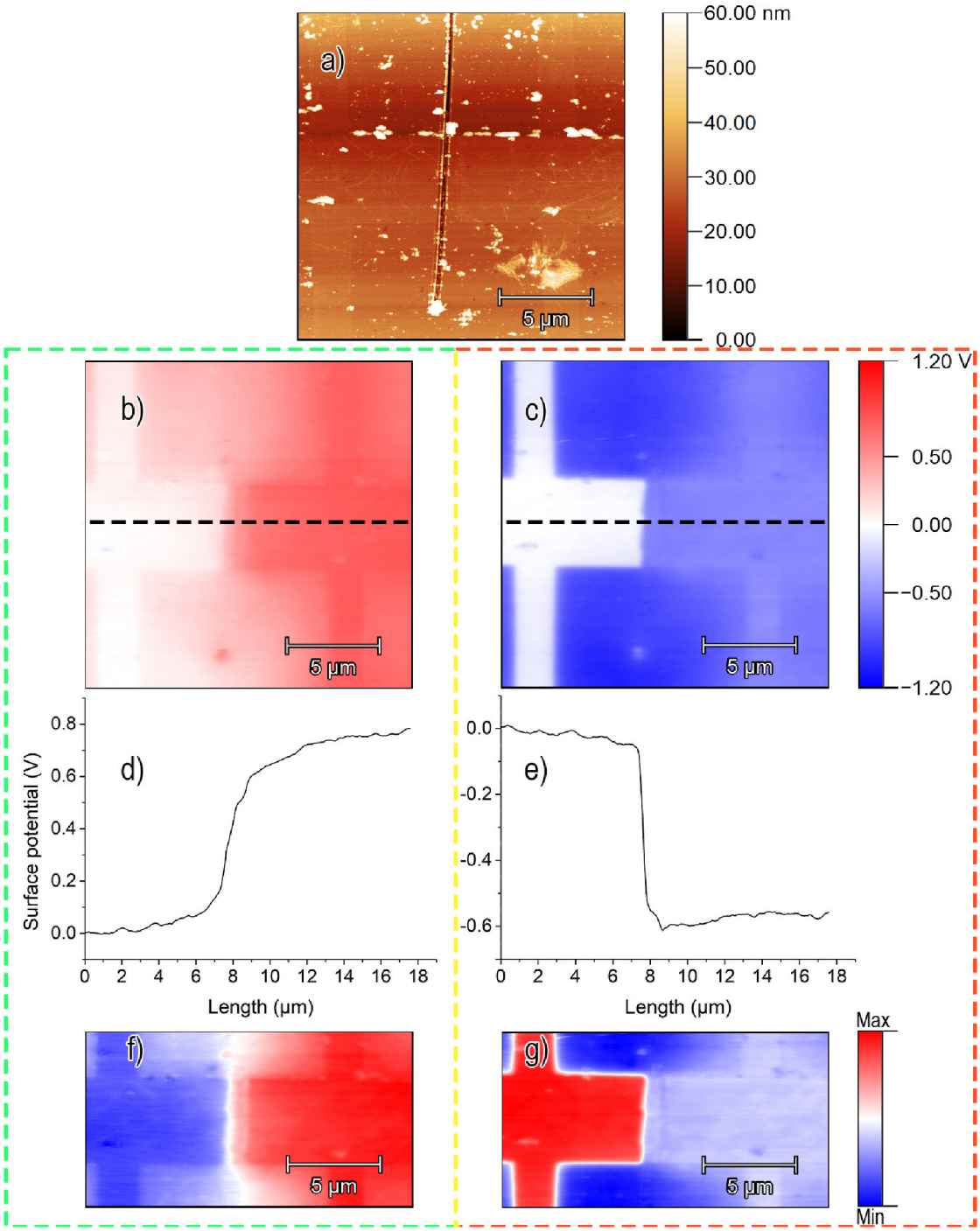

Fig. 3.10: Measurements after scratch: a) AFM topographic image of the damaged sample. [b) and c)]- KPFM images, where b) has the current source turned on from the right and c), where the current source is off. [d) and e)]- Surface potential profiles from the line marked by the black, segmented lines in b) and c), respectively. [f) and g)]- High contrast surface potential images corresponding to b) and c), respectively.

The damage can be observed in Fig. (3.10, a)), which clearly interrupts the

main channel of the Hall probe. The resistance of such a barrier was measured to be over 1000 GΩ at 3% RH. We can also observe the surface potential images measured by KPFM in Fig. (3.10, b) and c)). As the current source was still turned on in Fig. (3.10, b)), the surface potential on the source (left side of the main channel) is higher than on the drain, where the sample is electrically grounded. However, when the current source was turned off, the polarity of the background isolating substrate had a negative surface potential. This could have been caused by the volatile and damaged back gate, but such conclusions could not be determined as definite.

From even the high contrast images in Fig. (3.10, f) and g)), no second line can be observed, which was likely scraped away. However, the transport measurements did detect a change in resistance before the scratch occurred, with eleven valid data points indicating an increase from the previous $(2550 \pm 20)\,\Omega$ to $(4700 \pm 100)\,\Omega$. Due to the short lifetime of the second line, a more precise measurement was not possible.

The measured resistance with respect to time throughout the whole experiment can be observed in Fig. (3.11), where the attempts at lithography are pointed out.

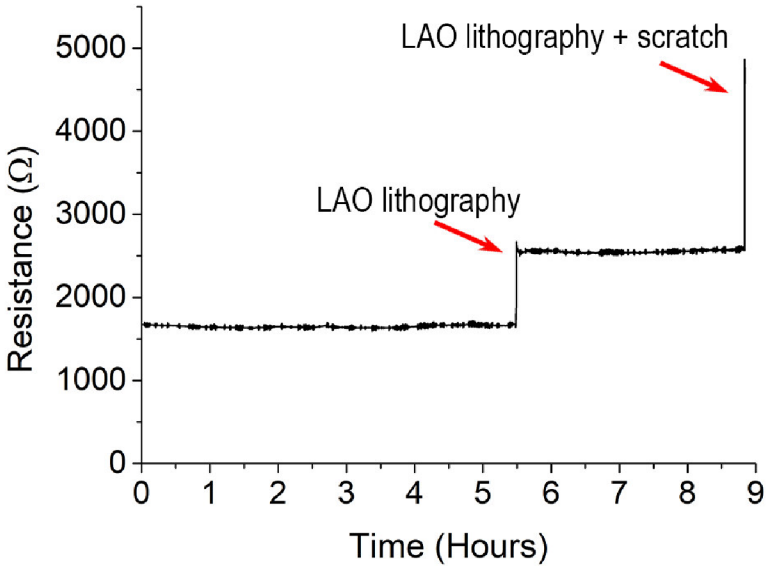

Fig. 3.11: Measured resistance of the graphene main channel with line interruptions with respect to time.

It is important to mention that the low feedback gain value (0.2) used during the experiment did not cause the damage. As there was no damage observed after the first line done by LAO lithography and the fact that the scratch extended beyond the bounds set for the lithography. However, a decision was made to increase the gain regardless for future experiments.

3.3.2 Constriction

In the second part of the results, we report on the to constriction of the main channel of the Hall probe structure, specifically in the area between the side channels. The original vision was to form a quantum point contact by constricting the main channel to the lowest possible diameter by forming two opposing triangular shapes with LAO lithography. However, due to the inability to form more complex shapes than lines and squares in the AFM infrastructure and the heavy drift of scanning, this goal was shifted in a different direction.

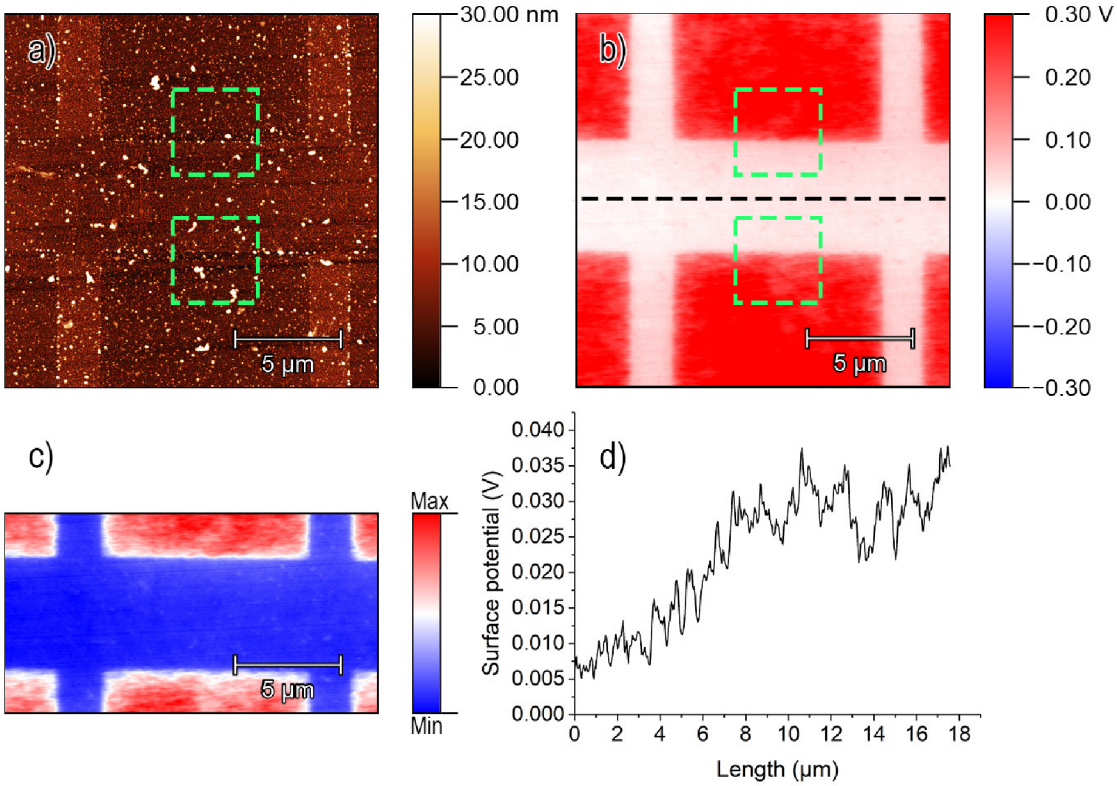

Fig. 3.12: Measurements done at 3% RH before lithography: a) AFM topographic image of the sample Hall probe structure, where the green, segmented squares represent the selection of the area for LAO lithography. b) KPFM image, where the electric current flows from the right side of the main channel, to the left. c) High-contrast image of the middle part of the Hall probe main channel. d) Line profile of the surface potential taken from the black segmented line in image b).

We elected to form a graphene constriction with a 2 µm width and 4 µm length in the vicinity of the main channel's middle area. This was to be done by oxidizing the graphene in two areas in the shape of squares, which oppose each other. The

selected location of the squares can be viewed in Fig. (3.12, a) and b)), where the scans were done under the same conditions as in Fig. (3.8), albeit on a new sample.

The positive surface potential of the SiO_2 substrate (observed in Fig. (3.12, b))) may have been caused by previous scans, because there is a tendency of tribelectric charging of the scanned area due to the friction between tip and sample area.

For LAO lithography in this experiment, some parameters were changed. Firstly, the RH was increased from the previous experiment's 55% to 65% during LAO. The bias voltage was also changed from −8 V to −9 V. Finally, the previously mentioned feedback gain was also increased from 0.2 to 0.4 in contact mode during lithography. After the lithography was done, the tips were changed back to NSG10 - Au probes, which were used to produce the scans in Fig. (3.13) at 3% RH.

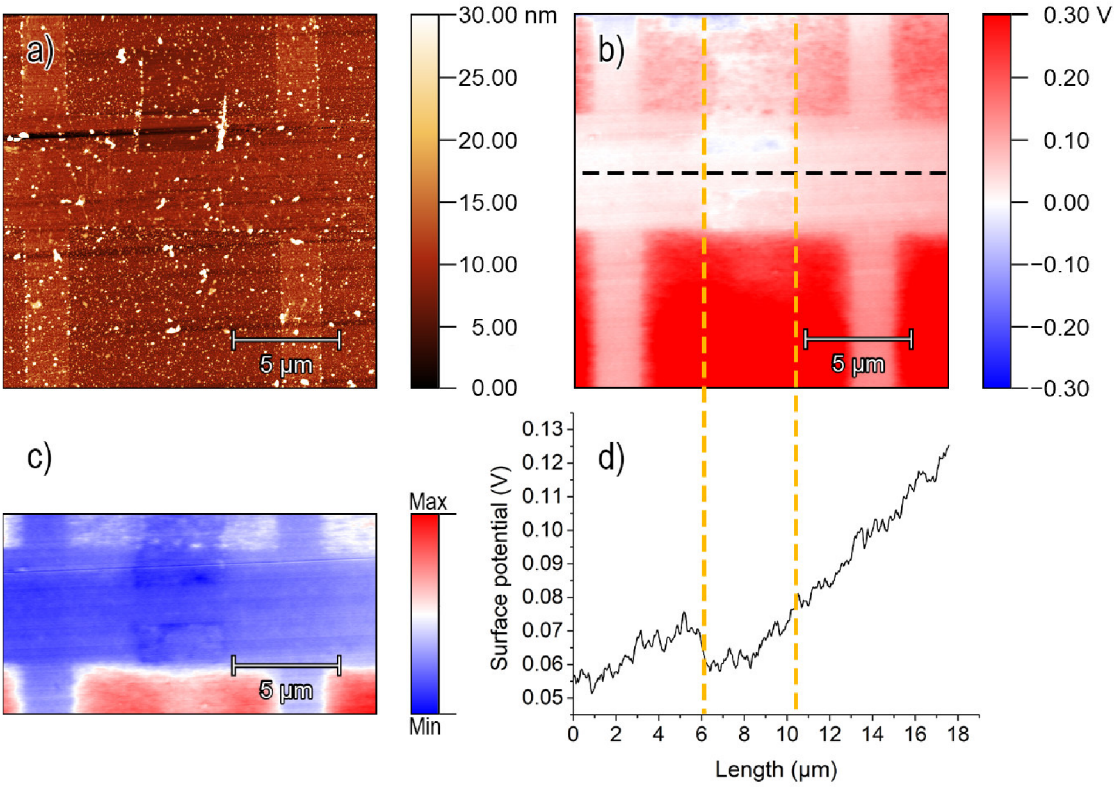

Fig. 3.13: Measurements done at 3% RH after lithography: a) AFM topographic image of the sample Hall probe structure. b) KPFM image, where the electric current flows from the right side of the main channel, to the left. c) High-contrast image of the middle part of the Hall probe main channel. d) Line profile of the surface potential taken from the black segmented line in image b).

In the AFM topography image in Fig. (3.13, a)), we can observe a significant difference compared to the image in Fig. (3.12, a)). This difference is merely a

relocation of contaminant particles, as there is still a visible step in height between the substrate and the graphene layer. The image therefore confirms that there was no major mechanical damage done to the graphene layer. The orange, segmented lines in images b) and d) in Fig. (3.13) are present to assist in seeing borders of the constricted portion of the main channel.

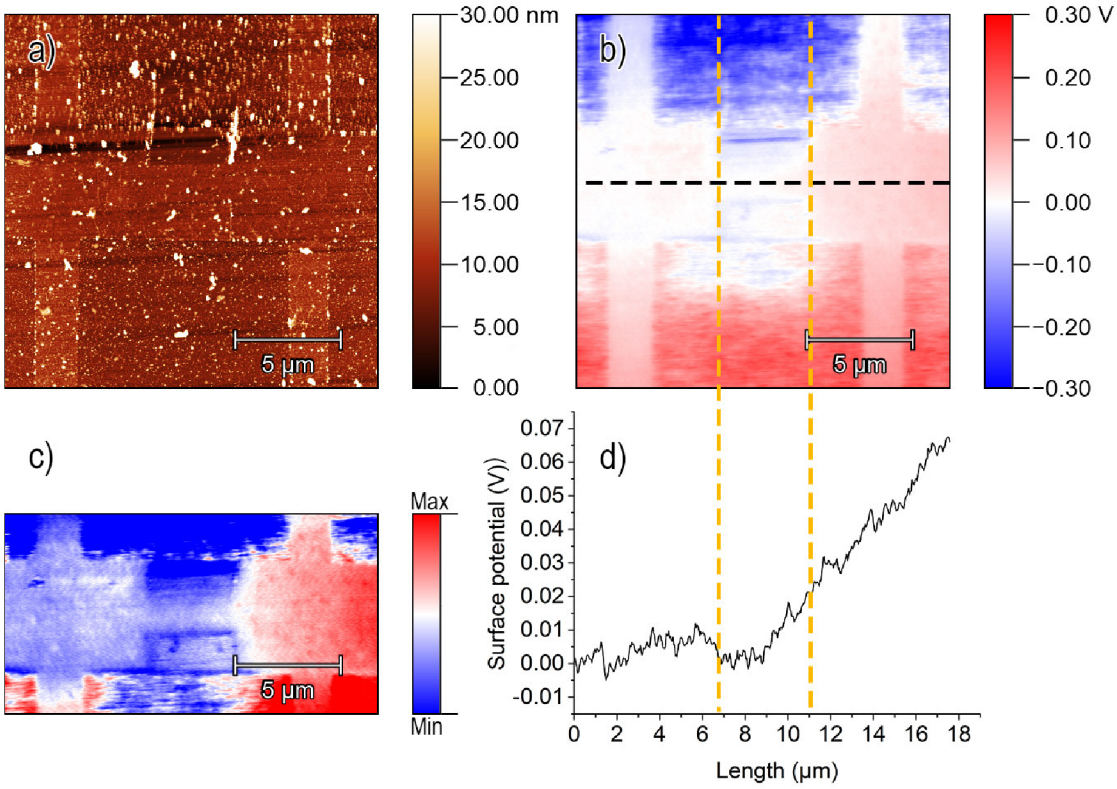

Fig. 3.14: Measurements done at 32% RH after lithography: a) AFM topographic image of the sample Hall probe structure. b) KPFM image, where the electric current flows from the right side of the main channel, to the left. c) High-contrast image of the middle part of the Hall probe main channel. d) Line profile of the surface potential taken from the black segmented line in image b).

It is important to mention, that the act of covering the AFM scanning head with the available humidity chamber is dangerous, as the immediate vicinity does not allow a large window of error (where bumping into the AFM head would cause major damage to the sample). This meant that the covering and uncovering of the AFM was done as little times as possible, meaning, that the first analytical scan in order after the lithography was the one depicted in Fig. (3.14). The scan in question was done without the use of the humidity chamber, thereby exposing the sample to the RH of the laboratory, which was 32%.

The higher surface potential seen on the isolating background substrate in Fig. (3.13, b)) can be explained as a consequence of scanning the sample priorly at the laboratory conditions seen in the scans presented in Fig. (3.14), which locally charged the scanned area. The lower potential seen between the top side channels, compared to the lower ones, in Fig. (3.14, b)), can be explained by the fact that the nano-voltmeter was connected to the contacts located at the top. This may have lowered the potential in the immediate area of the top graphene channels.

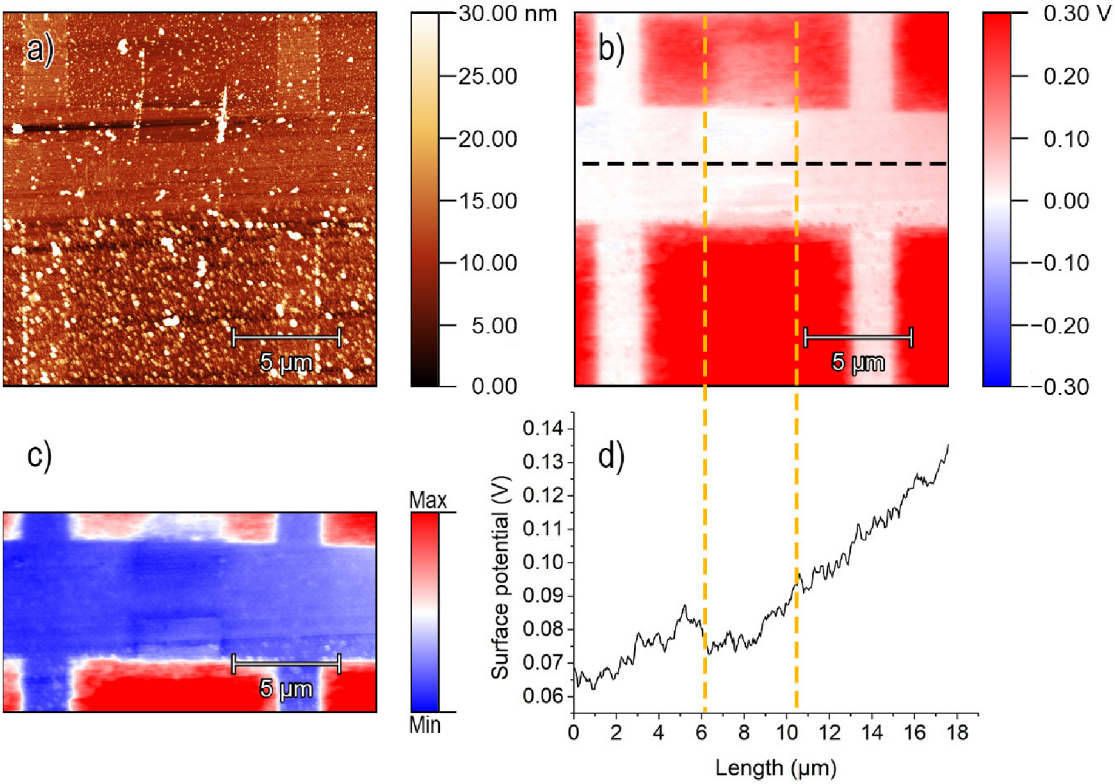

Fig. 3.15: Measurements done at 45% RH after lithography: a) AFM topographic image of the sample Hall probe structure. b) KPFM image, where the electric current flows from the right side of the main channel, to the left. c) High-contrast image of the middle part of the Hall probe main channel. d) Line profile of the surface potential taken from the black segmented line in image b).

The third scan after lithography was done at 45% RH, which can be seen in Fig. (3.15). However, this time the AFM cut into the sample a singular line horizontally through the main channel. As the cut was not overtly damaging, the only major difference was an increase in resistance. The cut's location can be seen in the topography and the high contrast images in Fig. (3.15, a) and c)). Since the damage was not sufficient in destroying the sample completely, the measurements

continued.

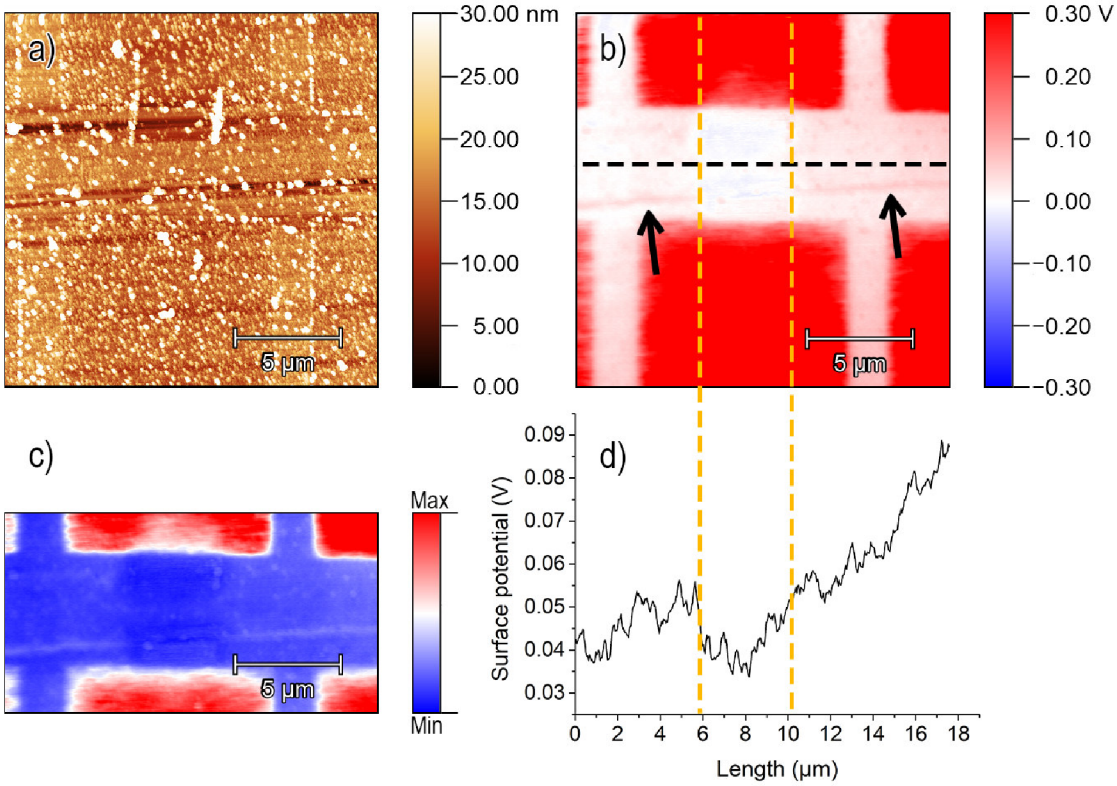

Fig. 3.16: Measurements done at 60% RH after lithography: a) AFM topographic image of the sample Hall probe structure. b) KPFM image, where the electric current flows from the right side of the main channel, to the left (where the black arrows mark the location of the scratch). c) High-contrast image of the middle part of the Hall probe main channel. d) Line profile of the surface potential taken from the black segmented line in image b).

The reliability of KPFM rapidly diminishes with increasing RH, as the resolution of the measurement decreases. Therefore, the resolution of the technique is also lower. As a result, the insulating barriers created by the graphene oxide tend to have less sharp and defined border, as can be seen in the high contrast image in Fig. (3.16, c)).

The resistance changes registered by the transport measurement setup were also recorded. Once again, the current was set to 100 nA and the resistance of the graphene sheet between the side channels was $(3840 \pm 15)\,\Omega$ at 3% RH. After the first square area was affected by LAO lithography, the resistance increased to $(5060 \pm 50)\,\Omega$ at 65% RH. With the formation of the second square, at 32% (laboratory conditions), the resistance stabilized at $(5690 \pm 10)\,\Omega$. By decreasing the RH, the resistance reduced as well to $(5600 \pm 10)\,\Omega$. Although the scratch in the Hall

structure heavily influenced the resistance of the system, the recorded value was $(10610 \pm 10)\,\Omega$ at 45% RH. Unexpectedly, further increase of RH to 60% lowered the resistance to $(10590 \pm 10)\,\Omega$.

The changes in resistance with respect to time can be seen in Fig. (3.17).

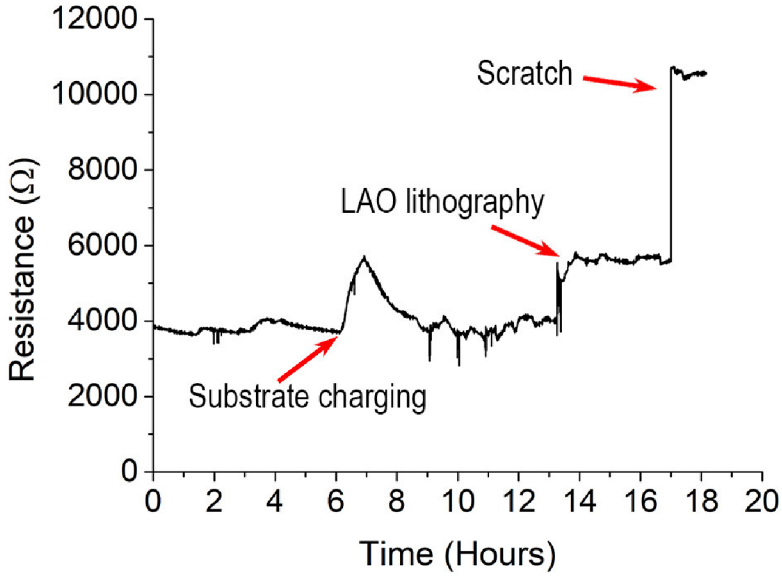

Fig. 3.17: Measured resistance of the graphene monolayer with a constriction between the side channels with respect to time.

The sharp increase in resistance marked by "Substrate charging" in Fig. (3.17) is not the actual measured resistance of the graphene layer, but an accidental measurement of voltage difference in the area near one of the contacted side channels connected to the nano-voltmeter. This voltage difference was induced by scanning the area near the side channel in tapping mode for testing reasons. After the charge dissipated, the resistance regained its original value over time. Ultimately, despite the challenges and issues faced, the constriction can be considered a success, because the flow of charge carriers was further limited by the oxidized graphene, which was observed both by KPFM and transport measurements.

3.3.3 Challenges

Problems arise in most projects. However, it is important to state their presence, as they leave clear paths where certain solutions may alter the direction of the end goals. In this part of the thesis, we will be detailing some of them, which may serve as an explanation for the routes taken for their navigation.

Firstly, the sample preparation is a challenging endeavour, which is heavily influenced by many factors, including, but not limited to: graphene sheet quality and integrity, substrate cleanliness, resist quality and the quality of machinery performing the necessary procedures. The main issue plaguing the device fabrication procedure was the cracking and tearing of the graphene layer. As such, the majority of the samples that were prepared were not functional. Only a very limited supply of four total Hall bars on two chips were available to us from the start of the project. However, the low amount of samples only increased the careful nature of our approach to the measurements and lithography and did not severely limit the project's potential.

Undoubtedly, the biggest challenges were the issues with the AFM. At first, the X-Y closed loop functionality was damaged. This meant that the system had to run in open loop, resulting in the fact that during scanning, the scanning field would shift over time and when the scanning window in the control software was moved to a certain area, the actual scanned area would not correspond. This meant that before any lithography could be made, the intended areas would have to be iteratively approached with multiple scans beforehand. The second issue was an inexplicable issue that arose upon the replacement of the AFM controller. The problem caused the probe tip to push into the sample during KPFM scanning and scratch the sample (see Fig. 3.10, a)). This did not happen during topography measurements, however, as the lithography is only properly visible in surface potential changes, it was necessary to accept a certain level of risk associated with KPFM.

When it comes to LAO lithography, the AFM probe's quality heavily influences its efficiency. More specifically, the conductive coating material at the end of the tip, which provides the necessary potential difference for oxidation. The biggest problem with the probes was the fact that material coating, like Au or TiN, rubbed off after a very short period of time, providing very little lithographic capability. As a result, we decided to use diamond coated probes, which had a higher wear resistance, at the cost of resolution. However, even using this alternative, some tips (even brand new ones) seemed to lack the conductive layer at the very tip. On the other hand, KPFM measurements were still possible with such tips.

The various limiting factors listed above meant that a trial period with practice samples was invaluable for the project. At first, cut Si (100) wafer samples (with a positive doping via boron) were used to test the oxidation method. These trial experiments were made easier with the fact that the oxidized Si (SiO_2) was visible in surface topography measurements, unlike graphene oxide. The extent of the present drift of the AFM was, therefore, thoroughly studied and compensated for in the final stages of our measurements. The drift within the individual scans was also corrected in post-processing using the polynomial method for distortions via

Gwyddion v. 2.58.

During transport measurements, in rare instances, the recorded resistance was infinity and negative infinity. These singular points were removed during the data processing phase, as they offered no physical meaning or purpose.

Although, the challenges were present throughout the project, the lithography was possible to test in the intended setup, utilizing both KPFM and the transport measurements.

Conclusion

To conclude a project is to write a certain number of words, describing the achieved goals and the methods used to achieve them, perhaps even provide some potential improvements to the techniques and usage for industrial purposes. Although that is the intention so far, it is also important to mention personal developments.

As most projects, ideal circumstances are rare. However, it is especially critical to persevere in the face of hardship and difficult situations. This is why we decided to move forward with the given experiments, even when we knew there was a chance of sample devaluation at any given moment during lithography or measurement. With the minimisation of human error, through practice and trials, the resulting experiments were considered a success in terms of local oxidation of graphene in a controlled manner.

The available research indicated the possibility of achieving our goals in a straightforward manner. However, the discrepancies in values and conditions within the literature seeded many doubts in their credibility and ultimately made it necessary to test the given methods on our own.

Using the given Hall probe samples, the effects of local oxidation could be monitored by measuring its transport capabilities in real time. With advanced measurement techniques, such as Kelvin probe force microscopy, the surface potential was measured in parallel. Simple line interruption of the Hall bar structure using oxidation was achieved successfully. Multiple interruptions were also attempted, which were briefly recorded straight after. Constriction of the structure's main channel was also a success, which was made possible by oxidizing larger areas of the sample in the shape of squares. The effect of relative humidity was additionally studied on the sample containing the constriction, where the charge propagation into the oxidized areas could be observed with increasing values.

In comparison with other studies, the project highlighted the necessity of picking a suitable probe type, which was critical for achieving oxidation on graphene. The settlement on diamond coated probes resulted in a lower resolution due to its larger tip apex radius, however, the higher wear resistance of the conductive coating material meant a more robust and reliable form of lithography.

The isolating abilities of the oxidized areas were limited, as reflected by the changes in resistance from transport measurements. However, the lithography method allowed a hands-on experience, with a less invasive nature, which may be preferred in sample preparation procedures that disallow resist usage.

To summarize, this master's thesis demonstrated the ability of an AFM to oxidize graphene. The effects were thoroughly studied and the various challenges were navigated. Although, room for improvement always exists, the experiments were

conducted to the best of our ability throughout the project.

Bibliography

[1] GEIM, A. K., et al. Van der Waals heterostructures. *Nature* [online]. 2013, **499**(7459), 419-425 [cit. 2023-05-26]. ISSN 0028-0836. Available from: doi:10.1038/nature12385.

[2] WALACE, P. The band theory of graphite. *Physical Review*, 1947, **71**, p. 622-634.

[3] CASTRO NETO, A. H., et al. The electronic properties of graphene. *Reviews of Modern Physics*. 2009, **81**(1), 109-162. ISSN 0034-6861. Available from: doi:10.1103/RevModPhys.81.109.

[4] TORRES, L. E. F. F., et al.: *Introduction to graphene-based nanomaterials: from electronic structure to quantum transport.* New York: Cambridge University Press, 2014. 409 p. ISBN 978-1-107-03083-1.

[5] MAFFUCCI, Antonio, et al. Electrical Properties of Graphene for Interconnect Applications. *Applied Sciences* [online]. 2014, **4**(2), 305-317 [cit. 2023-05-26]. ISSN 2076-3417. Available from: doi:10.3390/app4020305.

[6] ELETSKII, Aleksandr V, et al. Graphene: fabrication methods and thermophysical properties. *Physics-Uspekhi* [online]. 2011, **54**(3), 227-258 [cit. 2023-05-26]. ISSN 1063-7869. Available from: doi:10.3367/UFNe.0181.201103a.0233.

[7] NOVOSELOV, K. S., et al. Electronic properties of graphene. *Physica status solidi (b)* [online]. 2007, **244**(11), 4106-4111 [cit. 2023-05-26]. ISSN 03701972. Available from: doi:10.1002/pssb.200776208.

[8] BANSZERUS, Luca, et al. Ultrahigh-mobility graphene devices from chemical vapor deposition on reusable copper. *Science Advances* [online]. 2015, **1**(6), 6 [cit. 2023-05-26]. ISSN 2375-2548. Available from: doi:10.1126/sciadv.1500222.

[9] MATTEVI, Cecilia, et al. A review of chemical vapour deposition of graphene on copper. *J. Mater. Chem* [online]. 2011, **21**(10), 3324-3334 [cit. 2023-05-26]. ISSN: 0959-9428. Available from: doi:10.1039/C0JM02126A.

[10] GAHOI, Amit, et al. Contact resistance study of various metal electrodes with CVD graphene. *Solid-State Electronics* [online]. 2016, **125**, 234-239 [cit. 2023-05-26]. ISSN 00381101. Available from: doi:10.1016/j.sse.2016.07.008.

[11] GIESSIBL, Franz J. AFM's path to atomic resolution. *Materials Today* [online]. 2005, **8**(5), 32-41 [cit. 2023-05-26]. ISSN 13697021. Available from: doi:10.1016/S1369-7021(05)00844-8.

[12] ULAPANE, Sasanka et al. Atomic Force Microscopy-Based Static Plowing Lithography Using CaCO 3 Nanoparticle Resist Layers as a Substrate-Flexible Selective Metal Deposition Resist. *The Journal of Physical Chemistry C* [online]. 2021, **125**(42), 23490-23500 [cit. 2023-05-26]. ISSN 932-7447. Available from: doi:10.1021/acs.jpcc.1c07239.

[13] CHUNG, K. et al. Wear characteristics of diamond-coated atomic force microscope probe. *Ultramicroscopy* Elsevier B.V, **2007**, vol. 108(1), p. 1 – 10 [cit. 2021-5-17]. ISSN 0304-3991. Available from: doi:10.1016/j.ultramic.2007.01.016.

[14] Přikryl, V.: Selektivní hydrogenace/oxidace CVD grafenu pomocí AFM. Brno, 2017, Bakalářská práce (Bc.). VUT, Fakulta strojního in¾enýrství, Ústav fyzikálního inženýrství, 2017-06-09.

[15] MA, Y.-R., et al. Tip-induced local anodic oxidation on the native SiO 2 layer of Si(111) using an atomic force microscope. *Physical Review B* [online]. 2001, **64**(19), 5 [cit. 2023-05-26]. ISSN 0163-1829. Available from: doi:10.1103/PhysRevB.64.195324.

[16] GARCÍA, Ricardo, et al. Patterning of silicon surfaces with noncontact atomic force microscopy: Field-induced formation of nanometer-size water bridges. *Journal of Applied Physics* [online]. 1999, **86**(4), 1898-1903 [cit. 2023-05-26]. ISSN 0021-8979. Available from: doi:10.1063/1.370985.

[17] CHUANG, Min-Chiang, et al. Local anodic oxidation kinetics of chemical vapor deposition graphene supported on a thin oxide buffered silicon template. *Carbon* [online]. 2013, **54**, 336-342 [cit. 2023-05-26]. ISSN 00086223. Available from: doi:10.1016/j.carbon.2012.11.045.

[18] Tello, M., et al. *Applied Scanning Probe Methods IV - Industrial Applications.* Berlin: Springer. 2004, pp. 137–158. ISBN: 3-540-26912-6.

[19] GARCÍA, R. Dynamic atomic force microscopy methods. *Surface Science Reports* [online]. 2002, **47**(6-8), 197-301 [cit. 2023-05-26]. ISSN 01675729. Available from: doi:10.1016/S0167-5729(02)00077-8.

[20] BUH, G. H., et al. Real-time evolution of trapped charge in a SiO2 layer: An electrostatic force microscopy study. *Applied Physics Letters* [online]. 2001, **79**(13), 2010-2012 [cit. 2023-05-26]. ISSN 0003-6951. Available from: doi:10.1063/1.1404404.

[21] ZERWECK, U., et al. Accuracy and resolution limits of Kelvin probe force microscopy. *Physical Review*, **B71**, (2005), 125424.

[22] MELITZ, Wilhelm, et al. Kelvin probe force microscopy and its application. *Surface Science Reports* [online]. 2011, **66**(1), 1-27 [cit. 2023-05-26]. ISSN 01675729. Available from: doi:10.1016/j.surfrep.2010.10.001.

[23] SURPLICE, N A et al. A critique of the Kelvin method of measuring work functions. *Journal of Physics E: Scientific Instruments* [online]. 1970, **3**(7), 477-482 [cit. 2023-05-26]. ISSN 00223735. Available from: doi:10.1088/0022-3735/3/7/201.

[24] NONNENMACHER, M., et al. Kelvin probe force microscopy. *Applied Physics Letters* [online]. 1991, **58**(25), 2921-2923 [cit. 2023-05-26]. ISSN 0003-6951. Available from: doi:10.1063/1.105227.

[25] VENUGOPAL, Archana, et al. Effective mobility of single-layer graphene transistors as a function of channel dimensions. *Journal of Applied Physics* [online]. 2011, **109**(10), 6 [cit. 2023-05-26]. ISSN 0021-8979. Available from: doi:10.1063/1.3592338.

[26] HAN, Melinda Y., et al. Energy Band-Gap Engineering of Graphene Nanoribbons. *Physical Review Letters* [online]. 2007, **98**(20), 4 [cit. 2023-05-26]. ISSN 0031-9007. Available from: doi:10.1103/PhysRevLett.98.206805.

[27] KRUPKA, J. et al. Measurements of the sheet resistance and conductivity of thin epitaxial graphene and SiC films. *Applied Physics Letters* [online]. 2010, **96**(8), 3 [cit. 2023-05-26]. ISSN 0003-6951. Available from: doi:10.1063/1.3327334.

[28] G-MEZ-NAVARRO, Cristina, et al. Electronic Transport Properties of Individual Chemically Reduced Graphene Oxide Sheets. *Nano Letters* [online]. 2007, **7**(11), 3499-3503 [cit. 2023-05-26]. ISSN 1530-6984. Available from: doi:10.1021/nl072090c.

[29] KUMARI, Anita, et al. Electrical transport properties of polycrystalline CVD graphene on SiO2/Si substrate. *Diamond and Related Materials* [online]. 2014, **45**, 28-33 [cit. 2023-05-26]. ISSN 09259635. Availabe from: doi: 10.1016/j.diamond.2014.03.003.

[30] CHEN, Jian-Hao, et al. Intrinsic and extrinsic performance limits of graphene devices on SiO2. *Nature Nanotechnology* [online]. 2008, **3**(4), 206-209 [cit. 2023-05-26]. ISSN 1748-3387. Available form: doi: 10.1038/nnano.2008.58.

[31] BOLOTIN, K. I., et al. Temperature-Dependent Transport in Suspended Graphene. *Physical Review Letters* [online]. 2008, **101**(9), 4 [cit. 2023-05-26]. ISSN 0031-9007. Available from: doi:10.1103/PhysRevLett.101.096802.

[32] KONEČNÝ, Martin, et al. Kelvin Probe Force Microscopy and Calculation of Charge Transport in a Graphene/Silicon Dioxide System at Different Relative Humidity. *ACS Applied Materials & Interfaces* [online]. 2018, **10**(14), 11987-11994 [cit. 2023-05-26]. ISSN 1944-8244. Available from: doi:10.1021/acsami.7b18041.

[33] VASIC, Borislav, et al. Atomic force microscopy based manipulation of graphene using dynamic plowing lithography. *Nanotechnology* [online]. 2013, **24**(1), 9 [cit. 2023-05-26]. ISSN 0957-4484. Available from: doi:10.1088/0957-4484/24/1/015303.

[34] KUN, Péter, et al. Robust quantum point contact operation of narrow graphene constrictions patterned by AFM cleavage lithography. *Npj 2D Materials and Applications* [online]. 2020, **4**(1), 6 [cit. 2023-05-26]. ISSN 2397-7132. Available from: doi:10.1038/s41699-020-00177-x.

[35] GIESBERS, A.J.M., et al. Nanolithography and manipulation of graphene using an atomic force microscope. *Solid State Communications* [online]. 2008, **147**(9-10), 366-369 [cit. 2023-05-26]. ISSN 00381098. Available from: doi:10.1016/j.ssc.2008.06.027.

[36] WENG, Lishan, et al. Atomic force microscope local oxidation nanolithography of graphene. *Applied Physics Letters* [online]. 2008, **93**(9), 3 [cit. 2023-05-26]. ISSN 0003-6951. Available from: doi:10.1063/1.2976429.

[37] MASUBUCHI, S., et al. Fabrication of graphene nanoribbon by local anodic oxidation lithography using atomic force microscope. *Applied Physics Letters* [online]. 2009, **94**(8), 3 [cit. 2023-05-26]. ISSN 0003-6951. Available from: doi:10.1063/1.3089693.

[38] NEUBECK, Soeren, et al. Scanning probe lithography on graphene. *Physica status solidi (b)* [online]. 2010, **247**(11-12), 2904-2908 [cit. 2023-05-26]. ISSN 03701972. Available from: doi:10.1002/pssb.201000186.

[39] PUDDY, R. K., et al. Atomic force microscope nanolithography of graphene: Cuts, pseudocuts, and tip current measurements. *Applied Physics Letters* [online]. 2011, **98**(13), 3 [cit. 2023-05-26]. ISSN 0003-6951. Available from: doi:10.1063/1.3573802.

[40] BYUN, Ik-Su, et al. Nanoscale Lithography on Monolayer Graphene Using Hydrogenation and Oxidation. *ACS Nano* [online]. 2011, **5**(8), 6417-6424 [cit. 2023-05-26]. ISSN 1936-0851. Available from: doi:10.1021/nn201601m.

[41] MASUBUCHI, Satoru, et al. Atomic Force Microscopy Based Tunable Local Anodic Oxidation of Graphene. *Nano Letters* [online]. 2011, **11**(11), 4542-4546 [cit. 2023-05-26]. ISSN 1530-6984. Available from: doi:10.1021/nl201448q.

[42] LEE, Duk Hyun, et al. Fabricating in-plane transistor and memory using atomic force microscope lithography towards graphene system on chip. *Carbon* [online]. 2016, **96**, 223-228 [cit. 2023-05-26]. ISSN 00086223. Available from: doi:10.1016/j.carbon.2015.09.052.

[43] GARDENER, Jules A et al. Ice-assisted electron beam lithography of graphene. *Nanotechnology* [online]. 2012, **23**(18), 6 [cit. 2023-05-26]. ISSN 0957-4484. Available from: doi:10.1088/0957-4484/23/18/185302.

[44] SOMMER, Benedikt, et al. Electron-beam induced nano-etching of suspended graphene. *Scientific Reports* [online]. 2015, **5**(1), 5 [cit. 2023-05-26]. ISSN 2045-2322. Available from: doi:10.1038/srep07781.

[45] FAN, Jiyu, et al. Investigation of the influence on graphene by using electron-beam and photo-lithography. *Solid State Communications* [online]. 2011, **151**(21), 1574-1578 [cit. 2023-05-26]. ISSN 00381098. Available from: doi:10.1016/j.ssc.2011.07.028.

[46] VENUGOPAL, Gunasekaran et al. Temperature dependent transfer characteristics of graphene field effect transistors fabricated using photolithography. *Current Applied Physics* [online]. 2011, **11**(3), S381-S384 [cit. 2023-05-26]. ISSN 15671739. Available from: doi:10.1016/j.cap.2011.03.030.

[47] SHI, Runbo, et al. Scalable fabrication of graphene devices through photolithography. *Applied Physics Letters* [online]. 2013, **102**(11), 5 [cit. 2023-05-26]. ISSN 0003-6951. Available from: doi:10.1063/1.4795332.

[48] CHOI, Ahreum, et al. Residue-free photolithographic patterning of graphene. *Chemical Engineering Journal* [online]. 2022, **429**, 7 [cit. 2023-05-26]. ISSN 13858947. Available from: doi:10.1016/j.cej.2021.132504.

[49] BROWNSON, A. C., et al.: Graphene electrochemistry: an overview of potential applications. *Analyst*, 2010, **135**, p. 2768–2778. ISSN 0003-2654.

[50] SMITH, Anderson D., et al. Resistive graphene humidity sensors with rapid and direct electrical readout. *Nanoscale* [online]. 2015, **7**(45), 19099-19109 [cit. 2023-05-26]. ISSN 2040-3364. Available from: doi:10.1039/C5NR06038A.

[51] POPOV, V. I., et al. Graphene-based humidity sensors: the origin of alternating resistance change. *Nanotechnology* [online]. 2017, **28**(35), 10 [cit. 2023-05-26]. ISSN 0957-4484. Available from: doi:10.1088/1361-6528/aa7b6e.

[52] SCHEDIN, F., et al. Detection of individual gas molecules adsorbed on graphene. *Nature Materials* [online]. 2007, **6**(9), 652-655 [cit. 2023-05-26]. ISSN 1476-1122. Available from: doi:10.1038/nmat1967.

[53] CHEN, C. W., et al. Oxygen sensors made by monolayer graphene under room temperature. *Applied Physics Letters* [online]. 2011, **99**(24), 3 [cit. 2023-05-26]. ISSN 0003-6951. Available from: doi:10.1063/1.3668105.

[54] DAN, Yaping, et al. Intrinsic Response of Graphene Vapor Sensors. *Nano Letters* [online]. 2009, **9**(4), 1472-1475 [cit. 2023-05-26]. ISSN 1530-6984. Available from: doi:10.1021/nl8033637.

[55] BORINI, Stefano, et al. Ultrafast Graphene Oxide Humidity Sensors. *ACS Nano* [online]. 2013, **7**(12), 11166-11173 [cit. 2023-05-26]. ISSN 1936-0851. Available from: doi:10.1021/nn404889b.

[56] YOON, Hyeun Joong, et al. Carbon dioxide gas sensor using a graphene sheet. *Sensors and Actuators B: Chemical* [online]. 2011, **157**(1), 310-313 [cit. 2023-05-26]. ISSN 09254005. Available from: doi:10.1016/j.snb.2011.03.035.

Abbreviations

AFM	Atomic Force Microscope
AC	Alternating Current
BZ	Brillouin Zone
CVD	Chemical Vapor Deposition
DC	Direct Current
DCP	Diamond Coated Probe
EBL	Electron Beam Lithography
FET	Field Effect Transistor
HOPG	Highly Oriented Pyrolytic Graphite
IPA	Isopropyl Alcohol
KPFM	Kelvin Probe Force Microscopy
LAO	Local Anodic Oxidation
PMMA	Polymethyl methacrylate
RH	Relative Humidity
RIE	Reactive Ion Etching
UV	Ultraviolet

A Used AFM probes

	Diamond coated probe	Gold coated probe
Manufacturer	NT-MDT	AppNano
Model	DCP20	AN-NSG10/Au/50
Cantilever length (μm)	90	95
Cantilever width (μm)	60	30
Cantilever thickness (μm)	1.7 – 2.3	2
Resonant frequency (kHz)	260 – 630	250
Force constant (N/m)	28 – 91	11
Tip radius (nm)	50 – 70	<10
Tip height (μm)	10 – 15	14 – 16
Coat on reflective side	Gold (Au)	Gold (Au)
Coat on tip side	Diamond (thickness 70 nm)	Gold (Au)